remote sensing

MDPI

Article

When Deep Learning Meets Broad Learning: A Unified Framework for Change Detection with Synthetic Aperture Radar Images

Shuchen Yu [1], Zhulian Wang [2], Jiayi Qu [2], Xinxin Liu [2], Licheng Liu [2], Bin Yang [2,*] and Qiuhua He [1,3]

[1] Hunan Provincial Key Laboratory of Remote Sensing Monitoring of Ecological Environment in Dongting Lake Area, Hunan Center of Natural Resources Affairs, Changsha 410004, China
[2] School of Artificial Intelligence and Robotics, Hunan University, Changsha 410082, China
[3] Observation and Research Station of Lengshuijiang Mining Ecological Environmental Monitoring, Ministry of Natural Resources, Changsha 410004, China
* Correspondence: binyang@hnu.edu.cn

Highlights

What are the main findings?

- The proposed PC-BiBL framework successfully integrates a training-free Hierarchical Cross-feature Extraction (HCCE) module with a Bi-branch Broad Learning (BiBL) module to achieve high-accuracy change detection in bi-temporal SAR images.
- The method effectively eliminates the need for the complex and computationally intensive training process typically required by deep convolutional neural networks, while still extracting robust and discriminative hierarchical features.

What is the implication of the main finding?

- It presents an accurate and stable alternative to traditional deep learning models for SAR change detection, improving reliability and robustness in the detection process.
- The framework offers a robust and interpretable solution for analyzing remote sensing data, which can enhance the reliability of change monitoring applications in areas like urban planning, disaster assessment, and environmental monitoring.

Abstract

Change detection (CD) with synthetic aperture radar (SAR) images remains pivotal for environmental monitoring and disaster management. Deep learning has powerful feature extraction capabilities for CD, but suffers from complex architectures and limited interpretability. While BLSs demonstrate advantages in structural simplicity and interpretability, their feature representation capacity remains constrained. In high-precision CD with SAR images, strong feature representation capability is required, along with an uncomplicated framework and high interpretability. Therefore, a novel paradigm named PC-BiBL is proposed which achieves seamless integration of deep learning and broad learning. On the one hand, it employs a hierarchical cross-convolutional encoding (HCCE) module that uses pseudo-random cross-convolution (PCConv) for hierarchical cross-feature representation, aggregating contextual information. PCConv is an untrained convolution layer, which can utilize specialized pseudo-random kernels to extract features from bitemporal SAR images. On the other hand, since back-propagation algorithms are not required, the features can be directly fed into the bifurcated broad learning (BiBL) module for node expansion and direct parameter computation. BiBL constructs dual-branch nodes and computes their difference nodes, explicitly fusing bitemporal features while highlighting change information—an advancement over traditional BLS. Experiments on five SAR datasets demonstrate the

Check for updates

Academic Editor: Javier Marcello

Received: 15 November 2025
Revised: 19 December 2025
Accepted: 27 December 2025
Published: 1 January 2026

Copyright: © 2026 by the authors. Licensee MDPI, Basel, Switzerland. This article is an open access article distributed under the terms and conditions of the Creative Commons Attribution (CC BY) license.

state-of-the-art performance of PC-BiBL, surpassing existing methods in accuracy and robustness. Quantitative metrics and visual analyses confirm its superiority in handling speckle noise and preserving boundary information.

Keywords: broad learning; change detection (CD); deep learning; synthetic aperture radar (SAR)

1. Introduction

Change detection (CD) is a fundamental technique in remote sensing that involves analyzing images of the same geographical area acquired at different times to identify alterations in land surfaces [1–4]. This technique provides vital insights into land surface dynamics, supporting a wide range of applications [5], including environmental monitoring [6], forest management [7], and natural disaster assessment [8], etc. Synthetic aperture radar (SAR), an active remote sensing system, employs a narrow-band antenna to capture reflected signals from ground objects. Unlike optical imagery, SAR is unaffected by solar illumination or atmospheric conditions and can operate under all-weather and all-time conditions [9–11]. These advantages have made SAR-based CD a prominent research focus in the remote sensing community [12].

Over the past three decades, numerous algorithms have been developed for CD with SAR images. These algorithms can be broadly categorized into two groups: thresholding-based and clustering-based approaches. Although traditional methods achieved some success in early studies, more advanced approaches have been proposed in recent years to capture the complex spatial-frequency patterns in SAR images. For example, the frequency-spatial contextual awareness network (AIS-FCANet) integrates frequency-domain and spatial contextual information, significantly improving the capture of complex patterns [13]; dual-stream convolutional Transformer networks combine convolution and Transformer modules to extract local and global features, enhancing discriminative capability for multi-temporal SAR changes. Additionally, the multi-scale feature fusion CNN (MSF-CNN) utilizes multi-scale convolution modules to obtain hierarchical features, improving robustness to subtle changes and speckle noise [14]. These methods provide a more comprehensive background and theoretical basis for the proposed PC-BiBL framework, highlighting the importance of combining local and global features as well as multi-scale information when handling complex SAR image patterns.

However, such methods rely on feature engineering to extract shallow features, limiting their ability to capture intricate correlations within SAR images [15]. With the rapid advancement of computer technology, deep learning networks have emerged as a dominant approach in image processing, demonstrating remarkable proficiency in handling complex information [16–19]. Their ability to model intricate details has made them particularly effective for CD with SAR images. Examples include dual-channel convolutional neural networks (CNNs) for extracting deep features from parallel inputs [20], hybrid networks combining Transformer and UNet++ architectures to capture both local and global features [21], and deep nonsmooth nonnegative matrix factorization networks for learning hierarchical and localized representations [22]. These networks typically achieve discriminative feature extraction by optimizing parameters to minimize discrepancies between predictions and ground truth labels. However, when confronted with the complex patterns inherent in CD with SAR images, additional modules are often required. For instance, autoencoder-like structures have been introduced to map data into low-dimensional spaces [23], while graph neural networks have been employed to model local pixel struc-

tures using neighborhood blocks [24]. Networks often have limited interpretability and need complex architectures, necessitating frequent parameter adjustments in practical applications.

In contrast to deep learning networks, the broad learning system (BLS) has emerged as a novel learning paradigm characterized by its simplicity and high interpretability [25,26]. Designed to achieve broad and robust learning capabilities, BLSs have been successfully applied to diverse tasks, including landslide susceptibility mapping [27], wind turbine fault detection [28], and network interface flow prediction [29], etc. The classical BLS framework operates in three stages: (1) input data is mapped to generate feature nodes using nonlinear functions with random weights; (2) these feature nodes are further transformed into enhancement nodes through additional nonlinear mappings; and (3) the combined nodes are fed into the output layer, where weights are optimized via pseudoinverse computation to minimize errors and produce the final output [30]. The random initialization of weights in BLS enhances the nonlinearity and robustness of feature representation. In addition, since the weights of the output layer can be explicitly determined, the model is highly interpretable. For example, Feng and Chen [31] introduced fuzzy subsystems connected to enhancement nodes with random weights to improve nonlinear transformations and enhance interpretability. Hu et al. [32] designed a variational attention BLS to improve interpretability when handling data. Liu et al. [33] proposed regularized BLS which utilized Cauchy loss to address data [34] corrupted by Gaussian noise and outliers, thereby enhancing the interpretability of the framework. Despite these advancements, BLSs exhibit constrained feature expression capacity, particularly for tasks requiring the modeling of intricate correlations within data [35,36].

Therefore, it is clear that deep learning networks excel at extracting discriminative features, such as spatial relationships, texture, and spectral information [37–39], but often require complex architectures to process intricate data and have limited interpretability. In contrast, BLSs offer a robust and interpretable framework with simple structures [40], though they struggle to capture intricate feature relationships. Integrating a deep learning network with a BLS presents a promising solution for CD with SAR images. This hybrid approach leverages the strengths of both paradigms while mitigating their weaknesses. To be exact, the hybrid framework can achieve discriminative features with enhanced interpretability and reduced architectural complexity for high-precision CD with SAR images. However, the direct integration of a deep learning network with a BLS for CD with SAR images poses several challenges:

- Deep learning networks typically employ back-propagation algorithms to iteratively optimize parameters, whereas BLSs utilize pseudoinverse computation to directly derive output layer weights. This fundamental discrepancy complicates the integration of the two paradigms into a unified training framework, posing a critical barrier to their seamless combination.
- SAR imagery presents unique challenges for feature extraction due to its inherent speckle noise and temporal correlation effects. High-precision CD demands features that adapt to both spatial context variations across image regions and temporal evolution patterns between acquisition dates.
- Classical BLS architectures are a single-image processing paradigm which lacks explicit mechanisms for bi-temporal feature comparison, essential for identifying change patterns. The system must handle bi-temporal input and the complex temporal relationships inherent in CD with SAR images.

To solve the questions above, this paper proposes a novel unified framework, termed pseudo-random convolution with bifurcated broad learning (PC-BiBL), for CD with SAR images. PC-BiBL leverages untrained convolution with a bifurcated BLS mechanism to

achieve high-precision CD. The proposed framework consists of two core modules: a hierarchical cross-convolutional encoding (HCCE) module and a bifurcated broad learning (BiBL) module. The HCCE module employs pseudo-random cross-convolution (PCConv) to extract discriminative features, encompassing low-level features (e.g., edges and textures) at shallow layers and high-level features (e.g., object parts and shapes) at deeper layers. The PCConv block achieves feature smoothing through a mechanism that exhibits structural similarity to the local weighted averaging operation of traditional spatial filters. As the receptive field expands, this module effectively captures broader contextual information, thereby enhancing robustness against speckle noise. Notably, PCConv extracts cross-features with strong expressive capabilities without requiring a training process. The BiBL module maps these hierarchical features to generate sparse feature nodes and enhancement nodes, enhancing the nonlinearity and robustness of feature representation. Subsequently, difference nodes are computed to capture temporal discrepancies, a key adaptation that distinguishes this approach from classical BLSs and ensures compatibility with CD tasks. Finally, the difference nodes are fed into the output layer to predict the change map. The major contributions of this paper are summarized as follows:

- A novel unified framework is proposed for CD with SAR images, which is named PC-BiBL. It combines untrained pseudo-random convolution with a bifurcated BLS mechanism for CD with SAR images. PC-BiBL uniquely extracts features using a deep learning network and processes them through the BLS to generate change maps, offering a new direction for CD research.
- A HCCE module is introduced which adopts PCConv to extract discriminative features and explore correlations between bi-temporal images without requiring training. This process achieves feature smoothing and provides rich information for the BLS, distinguishing it from conventional convolution networks.
- A BiBL module is developed to generate bi-temporal nodes, analyze their variations, and enable the framework to effectively capture temporal changes in the SAR images. This adaptation enhances the compatibility of this framework with CD tasks, addressing limitations of classical BLSs.

The remainder of this paper is organized as follows: Section 2 details the architecture of PC-BiBL, Section 3 presents the datasets, experimental setups, and results, and Section 4 concludes the study.

2. Material and Methods

This section provides a comprehensive description of the proposed PC-BiBL framework, which comprises three key components: the overall architecture, the HCCE module, and the BiBL module.

2.1. Overall Architecture

The overall architecture of the proposed PC-BiBL framework, illustrated in Figure 1, integrates a deep learning network with a BLS for high-precision CD with SAR images. The workflow of PC-BiBL can be summarized as follows:

- In order to obtain hierarchical cross-features, a pair of SAR images, $T1$ and $T2$, are input into the HCCE module. This module utilizes PCConv to extract hierarchical spatial-temporal features without requiring a training process. These features are subsequently concatenated to generate hierarchical cross-features.
- The aforementioned PCConv is designed to extract deep cross-features by pseudo-random convolutions. The bi-temporal features and their difference feature are concatenated for clustering to extract k pixels. Then, these k pixels are then used to

derive pseudo-random kernels from the bi-temporal features, which are applied in the convolution process.

- A BiBL module is designed to obtain the final change map. All pairs of patches from the hierarchical cross-features are flattened as X^{t1} and X^{t2} and then are randomly mapped into bi-temporal nodes. The difference nodes are computed from these nodes and fed into the output layer to produce the change map.

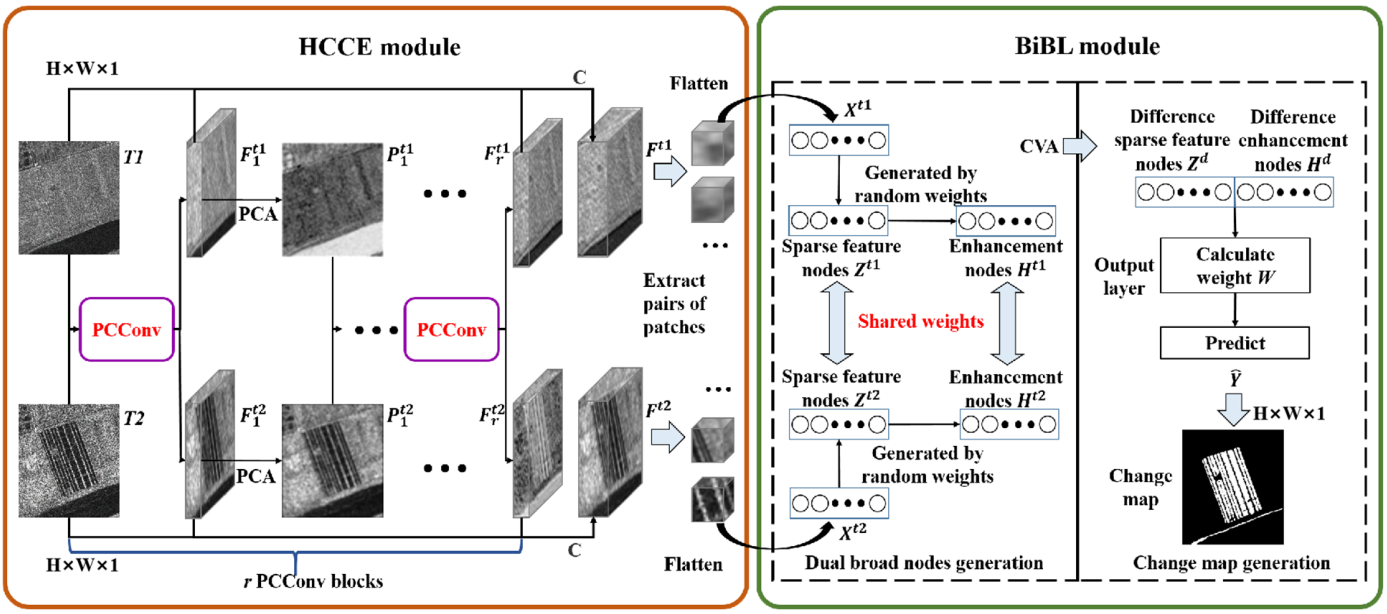


Figure 1. The overall architecture of the proposed PC-BiBL for CD with SAR images. It contains two modules, i.e., a HCCE module and BiBL module.

2.2. HCCE Module

In order to extract discriminative features for CD with SAR images, a HCCE module is designed. This module works without the need of training process and can minimize the intra-class difference and maximize the inter-class difference. It consists of two sub-modules, i.e., hierarchical feature extraction and PCConv.

2.2.1. Hierarchical Feature Extraction

Generally, shallow features capture fine-grained local information, such as edges, colors, and textures, while deep features represent coarse-grained semantic information, such as partial objects and whole shapes [41,42]. Combining features of varying depths, which encompass both fine-grained local and coarse-grained semantic information, is highly beneficial for CD. The HCCE module is designed to extract appropriate deep features by utilizing PCConv, a convolution mechanism specifically developed to eliminate the need for the training process inherent in traditional convolutional networks (which will be introduced in the following part). In addition, considering that the dimensions of obtained features increase tremendously with layers, principal components analysis (PCA) is adopted for dimensionality reduction [43]. Therefore, this module utilizes PCConv to obtain bi-temporal deep features and applies PCA between successive PCConv blocks to reduce dimensionality, thus facilitating efficient hierarchical feature extraction and reducing speckle noise. The process of generating hierarchical features is described as follows.

First, a pair of SAR images, $T1 \in \mathbb{R}^{H\times W\times 1}$ and $T2 \in \mathbb{R}^{H\times W\times 1}$, are fed into the first PCConv block. This block transforms $T1$ and $T2$ into bi-temporal features, F_1^{t1} and F_1^{t2}, i.e.,

$$\left(F_1^{t1}, F_1^{t2}\right) = \mathrm{PCConv}(T1, T2) \tag{1}$$

Second, the bi-temporal features, F_1^{t1} and F_1^{t2}, are reduced in dimensionality using PCA as follows:

$$P_1^{t1} = \mathrm{PCA}\left(F_1^{t1}\right) \tag{2}$$

$$P_1^{t2} = \mathrm{PCA}\left(F_1^{t2}\right) \tag{3}$$

where P_1^{t1} and P_1^{t2} denote the PCA-transformed features.

Third, P_1^{t1} and P_1^{t2} are fed to the next PCConv block, and the operation of PCConv block and PCA is repeated for $r-1$ times, by which F_2^{t1}, F_2^{t2}, …, F_{r-1}^{t1}, F_{r-1}^{t2}, and P_2^{t1}, P_2^{t2}, …, P_{r-1}^{t1}, P_{r-1}^{t2} are yielded. After that, P_{r-1}^{t1} and P_{r-1}^{t2} are fed to the rth PCConv block to get F_r^{t1} and F_r^{t2}, i.e.,

$$\left(F_r^{t1}, F_r^{t2}\right) = \mathrm{PCConv}\left(P_{r-1}^{t1}, P_{r-1}^{t2}\right) \tag{4}$$

Finally, the original image $T1$ is concatenated with features $F_1^{t1}, \ldots, F_r^{t1}$, to obtain the hierarchical features F^{t1}. Similarly, the original image $T2$ is concatenated with features $F_1^{t2}, \ldots, F_r^{t2}$, to get hierarchical features F^{t2}, i.e.,

$$F^{t1} = \mathrm{C}\left(T1, F_1^{t1}, \ldots, F_r^{t1}\right) \tag{5}$$

$$F^{t2} = \mathrm{C}\left(T2, F_1^{t2}, \ldots, F_r^{t2}\right) \tag{6}$$

where C denotes the concatenation in the channel dimension.

2.2.2. PCConv

CNNs are commonly used deep learning networks for CD with SAR images that employ convolution kernels to extract features by gliding over input data [44,45]. However, when processing intricate information, networks often need to add more modules, increasing architectural complexity and necessitating frequent parameter adjustments via back-propagation. Fortunately, a special convolution has been developed to bypass the training process in recent years. This convolution adopts image feature patches as convolution kernels to extract features. Once generated, these pseudo-random kernels remain fixed throughout the inference process. As a result, PCConv does not involve any learnable parameters, loss functions, or gradient-based optimization, and therefore does not require a training phase. For example, Xu et al. [46] adopted random image patches to extract features, and their findings indicated that using image patches as convolution kernels may offer enhanced robustness. Similarly, Ma et al. [47] extracted multiscale features through random patches taken from spatial features as convolution kernels. These studies highlight the effectiveness of using patches from original images or features as convolution kernels for discriminative feature extraction. Inspired by these studies, PCConv is proposed to extract cross-features by leveraging correlations within bi-temporal features. In particular, considering the similarities and differences of image feature patches, Simple Linear Iterative Clustering (SLIC) is adopted to cluster the input pixels to select pseudo-random patches as kernels, ensuring representativeness and differentiation [48]. Moreover, the kernels are shared across dual branches and applied to bi-temporal features, promoting intra-class aggregation and inter-class separation. This process achieves feature smoothing, which

functions similarly to a smoothing filter. The architecture of PCConv is depicted in Figure 2, and the process is as follows.

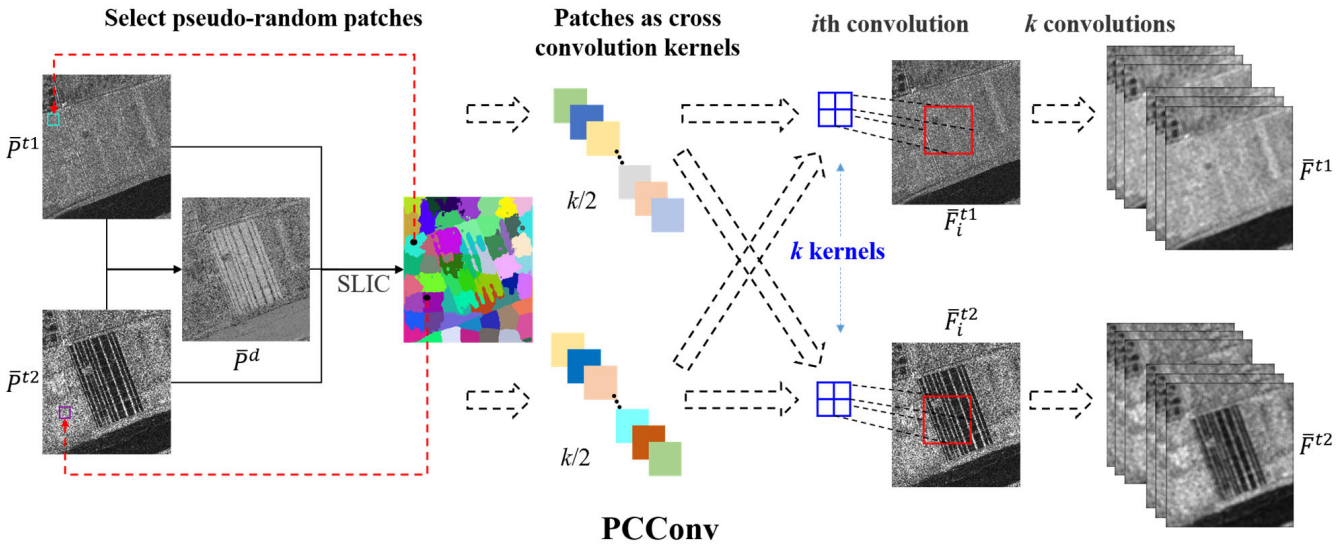


Figure 2. The architecture of PCConv, which adopts image feature patches as convolution kernels to extract deep cross-features.

Firstly, the input features, $\overline{P}^{t1}$ and $\overline{P}^{t2}$, with their difference feature $\overline{P}^{d}$ are concatenated and transformed into commission internationale eclairage lab (CIELAB) color mode, i.e.,

$$\overline{P} = \mathrm{CIELAB}\left(\mathrm{C}\left(\overline{P}^{t1}, \overline{P}^{t2}, \overline{P}^{d}\right)\right) \tag{7}$$

where $\overline{P}$ denotes the output feature of CIELAB color mode.

Then, feature $\overline{P}$ is fed into SLIC for pixel clustering. Particularly, to reduce boundary adherence and enhance intra-cluster similarity, the enforce label connectivity module is omitted. In the SLIC clustering process, the parameter k denotes the number of superpixels and controls the spatial scale of clustering. A larger k produces smaller and more fine-grained pixel clusters, preserving local structural details, while a smaller k results in larger and smoother clusters, enhancing regional consistency and noise suppression. Therefore, k balances detail preservation and feature smoothing. SLIC groups pixels into k clusters by calculating distance D between CIELAB color and xy-spatial space, i.e.,

$$D = \sqrt{d_c^2 + \frac{k(d_s m)^2}{N}} \tag{8}$$

where d_c denotes the distance of lab color, d_s denotes the distance of xy-space, m denotes the compactness parameter, and N denotes the number of pixels.

After extensive experiments across multiple SAR datasets, we found that $m = 80$ offers the best trade-off between spatial consistency and boundary preservation, especially under our modified setting without the boundary adherence term. Therefore, we adopt $m = 80$ as the default compactness parameter in PCConv.

After clustering, one pixel is randomly selected from each cluster, yielding k pixels. From these, $\frac{k}{2}$ s × s pseudo-random feature patches are extracted from feature $\overline{P}^{t1}$, and the remaining $\frac{k}{2}$ s × s patches are extracted from feature $\overline{P}^{t2}$. This can increase the representativeness of pseudo-random patches. Particularly, the k patches' center locations of in features $\overline{P}^{t1}$ and $\overline{P}^{t2}$ are the same as the locations of correspondingly selected k pixels.

Then, k pseudo-random feature patches are utilized as convolution kernels, producing cross-features in dual branches. Kernels in corresponding positions across branches share the same size and weights. The output cross-features are computed, i.e.,

$$\overline{F}_i^{t1} = \theta\left(\sum_{j=1}^{b} \overline{P}_j^{t1} \otimes Pa_j^i\right), i = 1, 2, \ldots, k \tag{9}$$

$$\overline{F}_i^{t2} = \theta\left(\sum_{j=1}^{b} \overline{P}_j^{t2} \otimes Pa_j^i\right), i = 1, 2, \ldots, k \tag{10}$$

where θ denotes the nonlinear activation function, $\otimes$ denotes the convolution function, b denotes the number of dimension of $\overline{P}^{t1}$ and $\overline{P}^{t2}$, $\overline{P}_j^{t1}$ is the jth dimension of $\overline{P}^{t1}$, $\overline{P}_j^{t2}$ denotes the jth dimension of $\overline{P}^{t2}$, Pa_j^i denotes the jth dimension of ith kernels, $\overline{F}_i^{t1}$ denotes the output of convolution with ith kernels from $\overline{P}^{t1}$, and $\overline{F}_i^{t2}$ denotes the output cross-features of convolution with ith kernels from $\overline{P}^{t2}$.

Finally, k convolutional outputs in dual branches are concatenated to produce the final cross-features $\overline{F}^{t1}$ and $\overline{F}^{t2}$, which are defined as follows:

$$F^{t1} = \mathrm{C}\left(\overline{F}_1^{t1}, \overline{F}_2^{t1}, \ldots, \overline{F}_k^{t1}\right) \tag{11}$$

$$F^{t2} = \mathrm{C}\left(\overline{F}_1^{t2}, \overline{F}_2^{t2}, \ldots, \overline{F}_k^{t2}\right) \tag{12}$$

2.3. BiBL Module

To improve robustness of feature representation and interpretability of model, BiBL module is designed. This module has the ability to broaden bi-temporal features and analyze their differences, making it compatible with CD task. The architecture of the BiBL module is shown in Figure 3. It can be divided into two parts, i.e., dual broad nodes generation and change map generation.

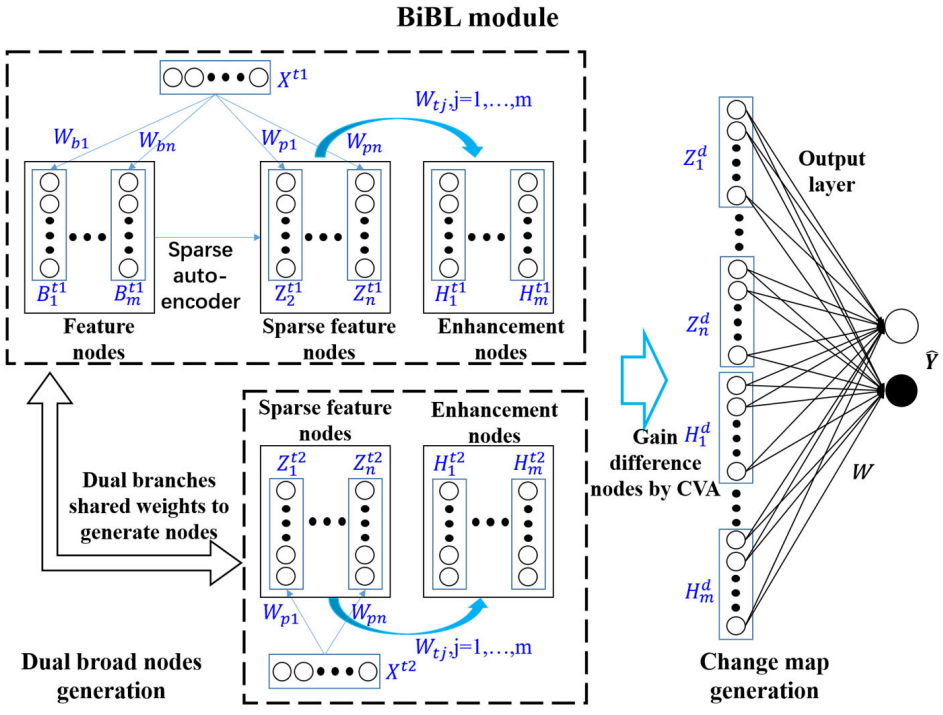


Figure 3. The architecture of the BiBL module.

2.3.1. Dual Broad Nodes Generation

The BLS is a novel learning paradigm without complicated structures, which can improve robustness and interpretability. This paper utilizes it to broaden hierarchical cross-features for the CD with SAR images tasks. Nevertheless, the classical BLS lacks the ability to broaden bi-temporal features, making it incompatible with this task. To this end, dual broad nodes generation is designed to get sparse feature nodes and enhancement nodes in dual branches, where the weights and biases are shared. In the dual broad learning (BiBL) module, sparse feature nodes select the most discriminative information to reduce redundancy, while enhancement nodes expand the feature space via random nonlinear mappings. Integrating both the sparse feature nodes and enhancement nodes provides expressive, and robust representations to help improve change detection performance. Additionally, to mitigate the randomness and instability inherent in node generation, a sparse autoencoder is utilized to create a more concise representation, facilitating the capture of the inner information.

First, given data X^{t1} in a branch, feature nodes B^{t1} can be calculated by random weights and biases. The ith feature node is defined, i.e.,

$$B_i^{t1} = \phi\left(X^{t1}W_{bi} + \beta_{bi}\right), i = 1, 2, \ldots, n \tag{13}$$

where B_i^{t1} denotes the ith feature node, ϕ denotes the nonlinear activation function, W_{bi} denotes the ith random weight, β_{bi} denotes the ith random bias, and n denotes the number of feature nodes.

Then, feature nodes $B^{t1} = \left[B_1^{t1}, B_2^{t1}, \ldots, B_n^{t1}\right]$ and the input data X^{t1} are fed into the sparse autoencoder for obtaining sparse feature nodes. In the sparse autoencoder, the alternating direction method of multipliers [49] is used to solve the optimization problem of getting sparse weights and biases. The optimization problem is as follows:

$$\arg\min_{w} f(w) + g(o), s.t.\ w - o = 0 \tag{14}$$

where $f(w) = \left\|B^{t1}w - X^{t1}\right\|_2^2$ and $g(o) = \eta\|w\|_1$. The solution of the optimization problem is by the iterative steps:

$$\begin{cases} w_{k+1} = \left((B^{t1})^T B^{t1} + \rho I\right)^{-1}\left((B^{t1})^T X^{t1} + \rho(o_k - u_k)\right) \\ o_{k+1} = S_{\frac{\eta}{\rho}}(w_{k+1} + u_k) \\ u_{k+1} = u^k + (w_{k+1} - o_{k+1}) \end{cases} \tag{15}$$

where $w = \left[W_p, \beta_p\right]$ is the concatenation of sparse weights W_p and biases β_p, $\rho > 0$, η is 0.001, and S denotes the soft threshholding operator. According to the experimental configuration used in the original BLS code, the sparse autoencoder optimization adopts a fixed iteration number of 50 to ensure stable convergence and sufficient sparsity. After 50 iterations to get sparse weights and biases, the ith sparse feature node can be obtained as follows:

$$Z_i^{t1} = \phi\left(X^{t1}W_{pi} + \beta_{pi}\right), i = 1, 2, \ldots, n \tag{16}$$

where Z_i^{t1} denotes the ith sparse feature node, ϕ denotes the nonlinear activation function, W_{pi} denotes the ith sparse weight, and β_{pi} denotes the ith sparse bias.

Then, enhancement nodes are mapped by sparse feature nodes $Z^{t1} = \left[Z_1^{t1}Z_2^{t1}, \ldots, Z_n^{t1}\right]$ with random weights and biases. The jth enhancement node is defined as follows:

$$H_j^{t1} = \sigma\left(Z^{t1}W_{tj} + \beta_{tj}\right), j = 1, 2, \ldots, m \tag{17}$$

where H_j^{t1} denotes the jth enhancement node, σ denotes the nonlinear activation function, W_{ti} denotes the jth random weight, β_{ti} denotes the jth random bias, and m denotes the number of enhancement nodes. Thus, enhancement nodes $H^{t1} = \left[H_1^{t1}, H_2^{t1}, \ldots, H_m^{t1}\right]$ are obtained.

In addition, given data X^{t2} in another branch, sparse feature nodes $Z^{t2} = \left[Z_1^{t2}, Z_2^{t2}, \ldots, Z_n^{t2}\right]$ and enhancement nodes $H^{t2} = \left[H_1^{t2}, H_2^{t2}, \ldots, H_m^{t2}\right]$ are calculated by the same W_p, β_p, W_t, and β_t.

Therefore, bi-temporal sparse feature nodes Z^{t1} and Z^{t2} and bi-temporal enhancement nodes H^{t1} and H^{t2} can be achieved in the generation of dual broad nodes.

The sparse autoencoder is introduced to enhance the discriminability and robustness of feature representations. By enforcing sparsity constraints, redundant information is suppressed while more change-sensitive features are emphasized, which is particularly beneficial for SAR images with strong noise and complex textures. The resulting sparse representation improves feature separability in the subsequent linear regression stage of the broad learning system, leading to better overall performance.

The sparsity-related parameters are selected by balancing feature expressiveness and sparsity, based on performance stability on the validation set, in order to avoid over-sparsification or insufficient representation capacity.

2.3.2. Change Map Generation

After generating the bi-temporal nodes, it is crucial to analyze their differences to identify change or its absence. Therefore, change map generation is designed to analyze the differences and generate a change map. Particularly, difference nodes are calculated by change vector analysis (CVA) to obtain differences [50] and then utilized for training the output layer by calculating pseudoinverse. The process of change map generation is interpretable, with the workflow proceeding as follows.

First, the bi-temporal sparse feature nodes Z^{t1} and Z^{t2} and bi-temporal enhancement nodes H^{t1} and H^{t2} are utilized to obtain difference nodes by CVA. Thus, difference sparse feature nodes Z^d and difference enhancement nodes H^d are acquired, i.e.,

$$Z^d = \mathrm{CVA}\left(Z^{t1}, Z^{t2}\right) \tag{18}$$

$$H^d = \mathrm{CVA}\left(H^{t1}, H^{t2}\right) \tag{19}$$

Second, for obtaining the output layer weight W to minimize the errors between outputs and label Y, the optimization problem can be defined as

$$\arg\min_{w} : \left\| \left[Z^d, H^d\right] W - Y \right\|_2^2 + \lambda \|W\|_2^2 \tag{20}$$

where λ denotes a constraint parameter for the sum of the squared weight. This problem is solved by the ridge regression approximation of pseudoinverse, which is the least square estimator of linear equations.

Finally, difference nodes Z^d and H^d are fed into the output layer to acquire the output and obtain the change map, i.e.,

$$\hat{Y} = \left[Z^d, H^d\right] W \tag{21}$$

where $\hat{Y}$ denotes the output, i.e., changed or unchanged.

3. Results

In order to evaluate the effectiveness of the proposed PC-BiBL, eight state-of-the-art models for CD with SAR images are adopted to compare with PC-BiBL. These eight models

are PCAKM [51], GarborPCA [52], NBRELM [53], CWNN [54], DDNet [55], LANTNet [56], M2HG [57], and WBANet [58]. Five widely used datasets, i.e., Yellow River I, Yellow River II, Yellow River III, Sulzberger, and San Francisco, are utilized to evaluate the performance of PC-BiBL compared with the eight models.

3.1. Dataset

In order to evaluate the effectiveness of PC-BiBL, five public bi-temporal SAR datasets are used in the experiments. Each datasets contains a $T1$ image which denotes the before changed images, a $T2$ image which denotes the after changed images, and a ground truth image, as shown in Figure 4. The first dataset shown in Figure 4a. is the Yellow River I dataset with the size of 257 × 289 pixels. The second dataset shown in Figure 4b, is the Yellow River II dataset with the size of 306 × 291 pixels. And the third dataset shown in Figure 4c, is the Yellow River III dataset with the size of 291 × 444 pixels. These three datasets are all selected from the Yellow River data, which consists of two 7688 × 7692 images that show the changes of the Yellow River from June 2008 to June 2009 captured by Radarsat-2. The fourth dataset is the Sulzberger dataset with the size of 256 × 256 pixels, as shown in Figure 4d. It is captured from the Sulzberger Ice Shelf, the data of which is obtained by the Envisat satellite of the European Space Agency on 11 March 2011 and 16 March 2011. The fifth dataset is the San Francisco dataset of 256 × 256 pixels, as shown in Figure 4e. It reflects on the changes of San Francisco from August 2003 to May 2004, and is obtained by the ERS-2 SAR sensor.

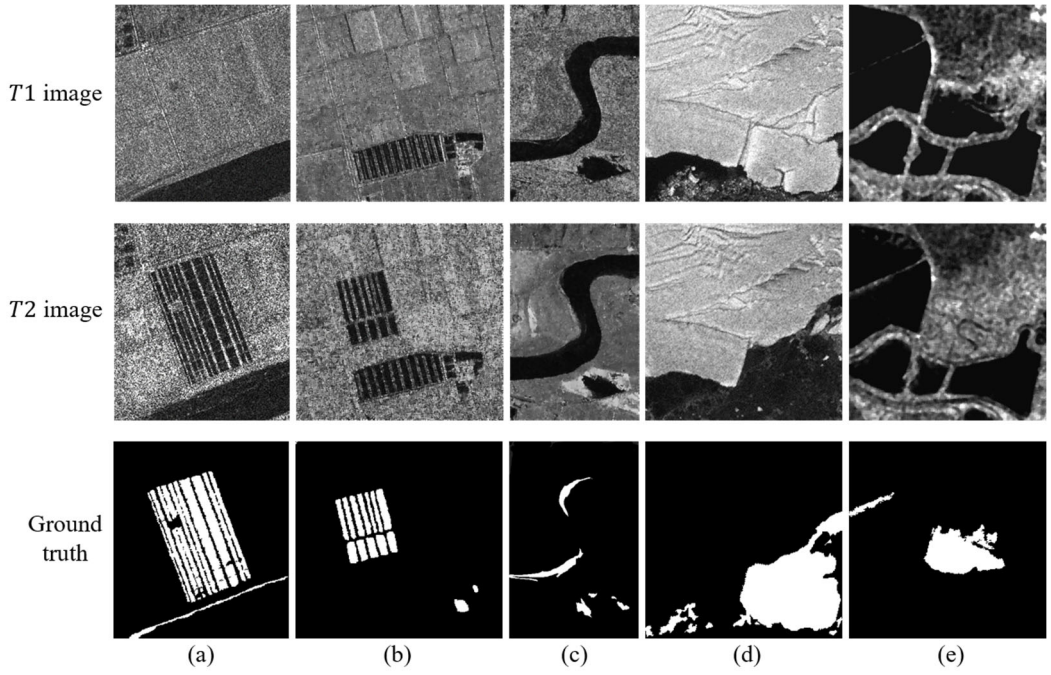


Figure 4. Five SAR image datasets. (**a**) Yellow River I, (**b**) Yellow River II, (**c**) Yellow River III, (**d**) Sulzberger, and (**e**) San Francisco. Every dataset contains image changed before ($T1$ image), image changed after ($T2$ image), and ground truth image.

3.2. Experimental Setup

Six evaluation indexes are adopted to analyze the performance of the proposed PC-BiBL, which contain overall error (OE), precision (P), Recall (R), F1-score (F1), overall accuracy (OA), and kappa coefficient (KC), defined as follows:

$$\mathrm{OE} = FP + FN \tag{22}$$

$$P = \frac{TP}{TP + FP} \tag{23}$$

$$R = \frac{TP}{TP + FN} \tag{24}$$

$$\mathrm{F1} = \frac{2 \times P \times R}{P + R} \tag{25}$$

$$\mathrm{OA} = \frac{TP + TN}{TP + FP + TN + FN} \tag{26}$$

$$\mathrm{KC} = \frac{\mathrm{OA} - \mathrm{PRE}}{1 - \mathrm{PRE}} \tag{27}$$

$$\mathrm{PRE} = \frac{(TP + FP)(TP + FN) + (FN + TN)(TN + FP)}{(TP + FP + TN + FN)^2} \tag{28}$$

where TP is true positive, TN is true negative, FN is false negative, and FP is false positive.

In the experiments, the HCCE module is configured with two PCConv blocks, each containing 50 feature channels, and the size of pseudo-random kernel in PCConv is set to 7×7, with half from the feature $\overline{P}^{t1}$ and the other half from the feature $\overline{P}^{t2}$. The kernels of the dual branches are shared to ensure consistency. Additionally, the BiBL module utilizes 11×11 patches as input. The number of sparse feature nodes is set to 4400, the number of enhancement nodes is set to 12,000, and the generating weights of dual nodes are shared.

All experiments were conducted on the same computer to ensure a consistent hardware environment and all compared models were evaluated on the same datasets with identical data preprocessing procedures and consistent network structure settings to guarantee fair comparisons. Due to differences in model architectures and training strategies, hyperparameters (e.g., learning rate, batch size, and regularization terms) were set according to the original papers or public implementations to ensure optimal performance for each model. The experiments were performed on a workstation equipped with an i9-12900K CPU and approximately 96 GB of system memory (94 GB available RAM). The models were implemented using PyTorch (version 1.13.0) and OpenCV (version 4.7.0.72) in the Python (version 3.7.13) development environment. No TensorFlow components were used.

3.3. Experiments on the Yellow River I Dataset

The statistical results of the experiments on the Yellow River I dataset are reported in Table 1. The results indicate that the proposed PC-BiBL outperforms the other eight models across multiple metrics, achieving an OE of 2052, R of 0.9662, F1 of 0.9267, OA of 0.9724, and KC of 0.9097. Although its P of 0.8940 is slightly lower than that of NBRELM, CWNN, and WBANet, the overall performance highlights the superiority of PC-BiBL in CD tasks. The visual results on the Yellow River I dataset, as depicted in Figure 5, further support these findings. The change maps generated by PCAKM, LANTNet, and M2HG contain numerous isolated pixels incorrectly predicted as changed, primarily due to the influence of speckle noise in SAR images. While GaborPCA, NBRELM, and WBANet demonstrate the ability to detect changed areas, they struggle to accurately delineate the precise boundaries of these regions. This limitation is reflected in their OA values, which are 0.0198, 0.0269, and 0.0074 lower than that of PC-BiBL, respectively. In contrast, the change map produced by PC-BiBL exhibits fewer erroneous isolated pixels and superior performance in detecting the boundaries of changed regions.

Table 1. CD results of the Yellow River I dataset.

Method	OE	P	R	F1	OA	KC
PCAKM	28,100	0.2788	0.6880	0.3968	0.6217	0.1877
GarborPCA	3524	0.8617	0.8787	0.8701	0.9526	0.7513
NBRELM	4045	0.9420	0.7447	0.8318	0.9455	0.7583
CWNN	2483	0.9312	0.8801	0.9050	0.9666	0.8412
DDNet	5709	0.7588	0.8429	0.7986	0.9231	0.7997
LANTNet	5651	0.7496	0.8699	0.8053	0.9239	0.8848
M2HG	4355	0.8607	0.8062	0.8326	0.9414	0.7971
WBANet	2601	**0.9510**	0.8502	0.8978	0.9650	0.8767
PC-BiBL	**2052**	0.8904	**0.9662**	**0.9267**	**0.9724**	**0.9097**

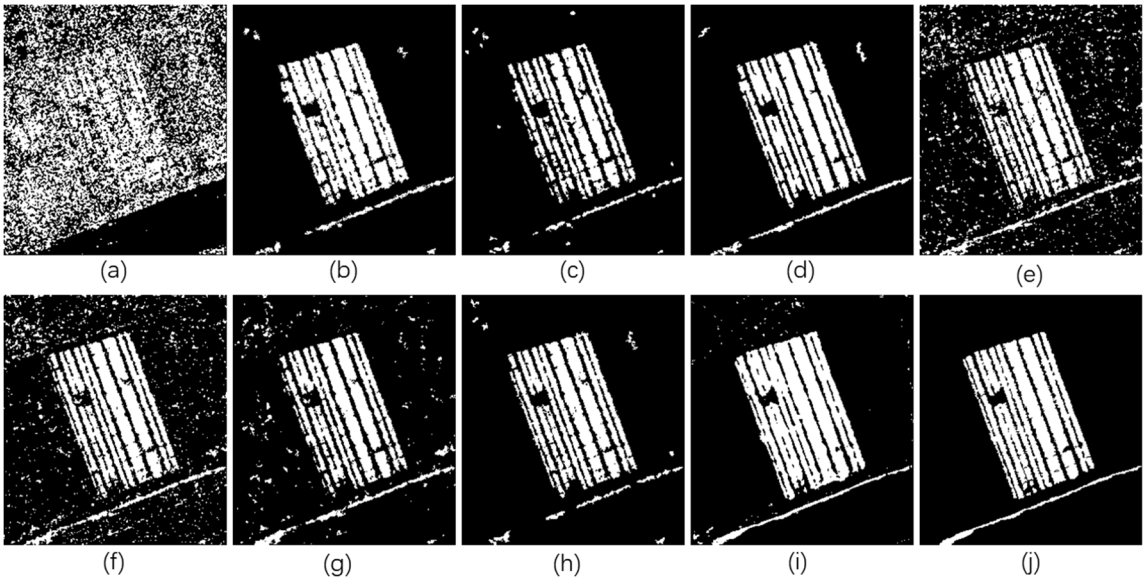


Figure 5. CD results of the Yellow River I dataset. (**a**) PCAKM, (**b**) GarborPCA, (**c**) NBRELM, (**d**) CWNN, (**e**) DDNet, (**f**) LANTNet, (**g**) M2HG, (**h**) WBANet (**i**) PC-BiBL, and (**j**) ground truth.

3.4. Experiments on the Yellow River II Dataset

Table 2 displays the statistical results for the proposed PC-BiBL and the compared models on the Yellow River II dataset. The results demonstrate that PC-BiBL achieves superior performance across most evaluation metrics, except for P. Notably, PC-BiBL achieves a KC of 0.9010, which is widely recognized as one of the most robust and reliable evaluation metrics for CD tasks. This KC value is higher than that of the other eight CD models, underscoring the superior performance and reliability of PC-BiBL in accurately detecting changes. Although GaborPCA achieves the highest P of 0.9871, it incorrectly predicts 282 more pixels than PC-BiBL. This discrepancy results in GaborPCA having a R that is 0.2327 lower, an F1 that is 0.0518 lower, and a KC that is 0.0806 lower compared to PC-BiBL. The change maps generated by the models, along with the ground truth for the Yellow River II dataset, are illustrated in Figure 6. The change maps produced by PCAKM, CWNN, DDNet, and LANTNet exhibit numerous isolated pixels erroneously predicted as changed, primarily due to the influence of noise and model limitations. For GaborPCA and NBRELM, while they are capable of detecting changed regions, accurately delineating the boundaries of these areas remains challenging, leading to an increase in incorrectly predicted unchanged pixels. In contrast, the change map generated by PC-BiBL contains fewer errors, particularly in detecting locally consistent changed pixels. Although PC-BiBL occasionally misclassifies a few unchanged boundary pixels, its overall performance in CD is significantly better, particularly in detecting changed pixels with local consistency.

Table 2. CD results of the Yellow River II dataset.

Method	OE	P	R	F1	OA	KC
PCAKM	17,770	0.2248	0.9691	0.3650	0.8004	0.2974
GarborPCA	1344	**0.9871**	0.7548	0.8555	0.9849	0.8204
NBRELM	2017	0.9842	0.6273	0.7663	0.9773	0.8180
CWNN	1145	0.9082	0.8708	0.8891	0.9871	0.8476
DDNet	1746	0.8489	0.8135	0.8308	0.9804	0.7544
LANTNet	1802	0.8303	0.8271	0.8287	0.9798	0.8819
M2HG	1689	0.8341	0.8482	0.8411	0.9810	0.8310
WBANet	1286	0.9112	0.8376	0.8728	0.9856	0.8652
PC-BiBL	**1063**	0.8392	**0.9875**	**0.9073**	**0.9881**	**0.9010**

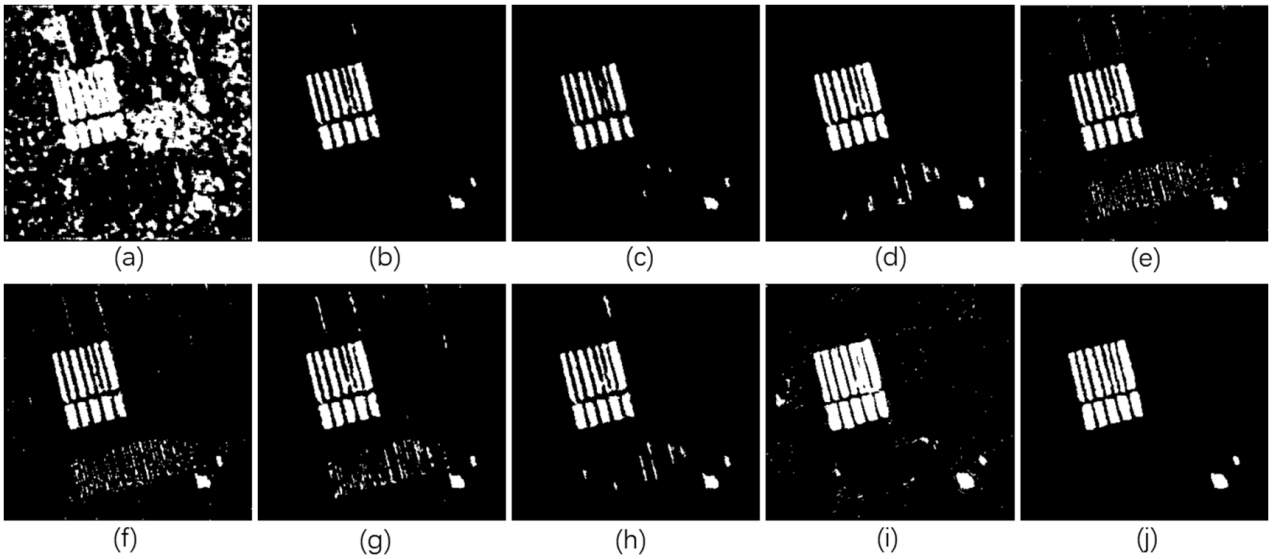


Figure 6. CD results of the Yellow River II dataset. (**a**) PCAKM, (**b**) GarborPCA, (**c**) NBRELM, (**d**) CWNN, (**e**) DDNet, (**f**) LANTNet, (**g**) M2HG, (**h**) WBANet (**i**) PC-BiBL, and (**j**) ground truth.

3.5. Experiments on the Yellow River III Dataset

The evaluation indexes for all models on the Yellow River III dataset are represented in Table 3. The proposed PC-BiBL outperforms the other eight models in terms of OE, R, F1, OA, and KC. Although its P is not the highest, PC-BiBL achieves a R of 0.9934, surpassing other models by more than 0.1076, demonstrating that the proposed PC-BiBL performs better in accurately detecting truly changed pixels. The strong performance of PC-BiBL in CD can be attributed to its effective trade-off between P and R, as well as its low OE value. Visible experimental results for these models on the Yellow River III dataset are given in Figure 7. Among the models, PCANet exhibits unsatisfactory performance in its change map due to the influence of speckle noise. The change map generated by LANTNet contains a relatively higher number of incorrectly predicted isolated pixels. GaborPCA and NBRELM struggle to accurately detect changed pixels near the boundaries. While CWNN and WBANet achieve reasonable CD results with few errors, their change maps lack precision in delineating the boundaries of changed regions, resulting in 44 and 118 more OE compared to PC-BiBL. In contrast, although PC-BiBL also produces a few isolated errors, it provides more detailed and precise boundary information, highlighting its robustness and accuracy in capturing fine-grained changes.

Table 3. CD results of the Yellow River III dataset.

Method	OE	P	R	F1	OA	KC
PCAKM	62,237	0.0052	0.0712	0.0096	0.5183	−0.0551
GarborPCA	1813	**0.8309**	0.7206	0.7718	0.9860	0.7646
NBRELM	1892	0.8238	0.7065	0.7606	0.9854	0.7531
CWNN	1650	0.7728	0.8672	0.8173	0.9872	0.8107
DDNet	1921	0.7342	0.8597	0.7920	0.9851	0.7844
LANTNet	2297	0.6754	0.8858	0.7664	0.9822	0.7574
M2HG	2276	0.6836	0.8658	0.7640	0.9824	0.7550
WBANet	1724	0.7676	0.8531	0.8081	0.9867	0.8012
PC-BiBL	**1606**	0.7282	**0.9934**	**0.8404**	**0.9876**	**0.8344**

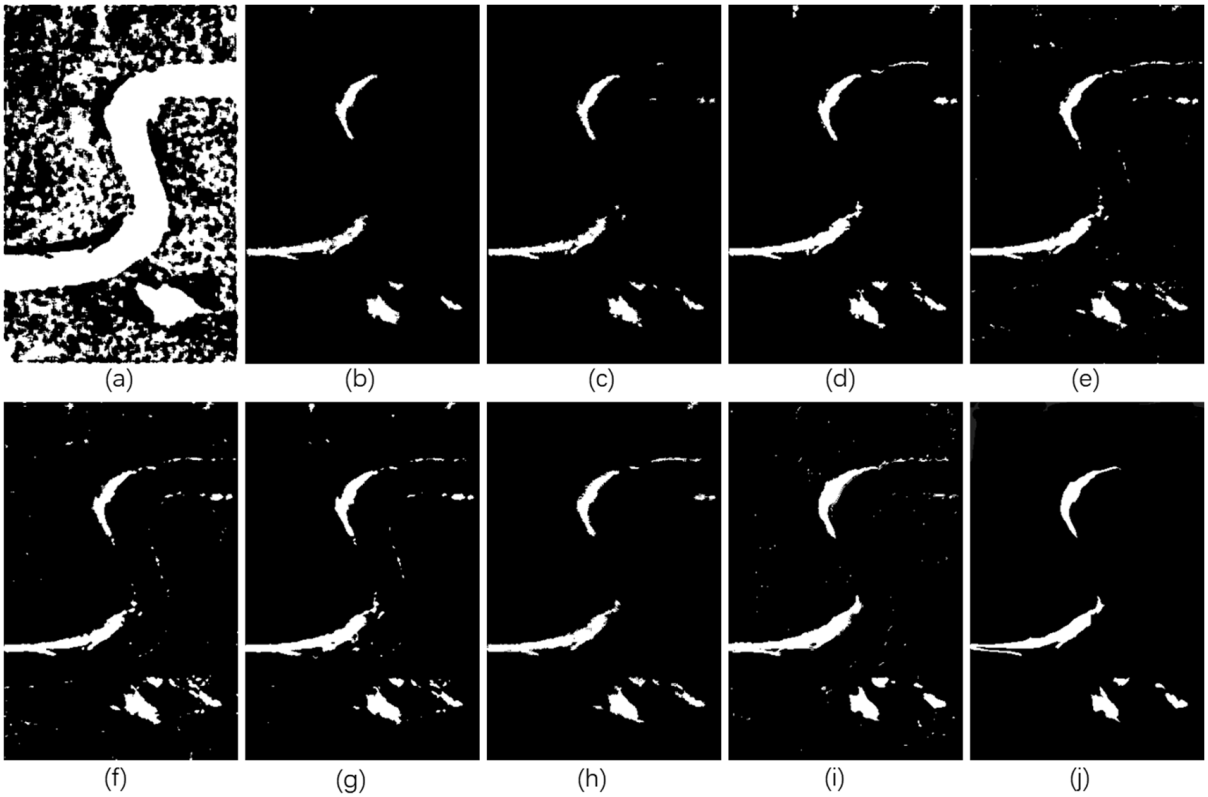


Figure 7. CD results of the Yellow River III dataset. (**a**) PCAKM, (**b**) GarborPCA, (**c**) NBRELM, (**d**) CWNN, (**e**) DDNet, (**f**) LANTNet, (**g**) M2HG, (**h**) WBANet (**i**) PC-BiBL, and (**j**) ground truth.

3.6. Experiments on the Sulzberger Dataset

Statistical results of CD on the Sulzberger dataset are reported in Table 4. From the datasets shown in Figure 4, the Sulzberger dataset exhibits lower levels of speckle noise compared to the other datasets, contributing to relatively high CD accuracies across models. Although CWNN achieves the highest P of 0.9716 and M2HG attains the highest R of 0.9865, the proposed PC-BiBL demonstrates superior performance in terms of comprehensive evaluation metrics, achieving the highest F1 of 0.9715, OA of 0.9889, and KC of 0.9647. The change maps on the Sulzberger dataset are shown in Figure 8. Models such as PCAKM, NBRELM, DDNet, and M2HG exhibit difficulties in accurately recognizing changes in the lower-left corner of the Sulzberger dataset. In addition, some models struggle to precisely detect certain pixels within the changing regions, particularly for GaborPCA, NBRELM, LANTNet, DDNet, M2HG, and WBANet. However, the change map generated by the proposed PC-BiBL contains significantly fewer incorrectly predicted pixels, demonstrating its superior ability to accurately capture changes while minimizing errors.

Table 4. CD results of the Sulzberger dataset.

Method	OE	P	R	F1	OA	KC
PCAKM	1730	0.9588	0.9016	0.9293	0.9736	0.9131
GarborPCA	1006	0.9662	0.9536	0.9598	0.9846	0.9462
NBRELM	1027	0.9466	0.9735	0.9598	0.9843	0.9559
CWNN	804	**0.9716**	0.9645	0.9680	0.9877	0.9502
DDNet	1113	0.9375	0.9768	0.9568	0.9830	0.9500
LANTNet	898	0.9646	0.9642	0.9644	0.9863	0.9603
M2HG	927	0.9426	**0.9865**	0.9641	0.9859	0.9553
WBANet	871	0.9655	0.9654	0.9655	0.9867	0.9572
PC-BiBL	**725**	0.9628	0.9804	**0.9715**	**0.9889**	**0.9647**

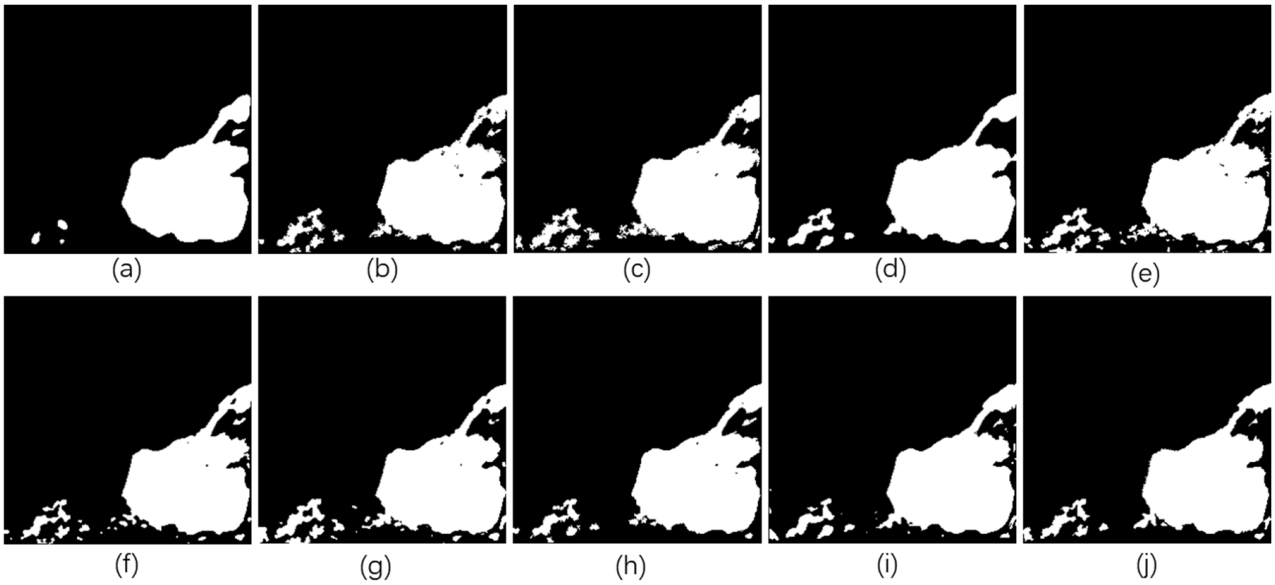


Figure 8. CD results of the Sulzberger dataset. (**a**) PCAKM, (**b**) GarborPCA, (**c**) NBRELM, (**d**) CWNN, (**e**) DDNet, (**f**) LANTNet, (**g**) M2HG, (**h**) WBANet (**i**) PC-BiBL, and (**j**) ground truth.

3.7. Experiments on the San Francisco Dataset

The results on the San Francisco dataset are given in Table 5. The proposed PC-BiBL demonstrates superior performance compared to other models, achieving an F1 of 0.9354, an OA of 0.9902, and a KC of 0.9901, which collectively evaluate the overall CD performance. Notably, only 645 pixels are mispredicted by PC-BiBL on this dataset. Although its P is slightly lower, PC-BiBL achieves an exceptionally high R of 0.9962, indicating its strong capability in accurately identifying truly changed pixels. The binary change maps of the San Francisco dataset are shown in Figure 9. PCANet and WBANet exhibit unsatisfactory performance compared to other models, with both incorrectly identifying numerous unchanged pixels as changed. GaborPCA and NBRELM fail to detect changes in the upper-left corner of the image. Additionally, CWNN, DDNet, LANTNet, M2HG, and WBANet perform inadequately in delineating the boundaries of changed regions. The change map generated by LANTNet contains a significant number of incorrectly predicted isolated pixels. Although the proposed PC-BiBL exhibits minor inaccuracies in predicting a few unchanged boundary pixels, it outperforms all other models in detecting changed pixels with greater precision. Furthermore, Table 5 and Figure 9 demonstrate that PC-BiBL produces the fewest mispredictions, highlighting its accuracy in handling CD tasks.

Table 5. CD results of the San Francisco dataset.

Method	OE	P	R	F1	OA	KC
PCAKM	8270	0.3535	0.9229	0.5112	0.8738	0.4548
GarborPCA	878	**0.9791**	0.8303	0.8986	0.9866	0.8647
NBRELM	914	0.9784	0.8231	0.8940	0.9861	0.8247
CWNN	713	0.9108	0.9398	0.9251	0.9891	0.8914
DDNet	1200	0.8570	0.8928	0.8746	0.9817	0.8870
LANTNet	1634	0.7821	0.9027	0.8381	0.9751	0.9191
M2HG	877	0.8825	0.9377	0.9092	0.9866	0.9020
WBANet	5842	0.4410	0.9221	0.5966	0.9109	0.5534
PC-BiBL	**645**	0.8816	**0.9962**	**0.9354**	**0.9902**	**0.9301**

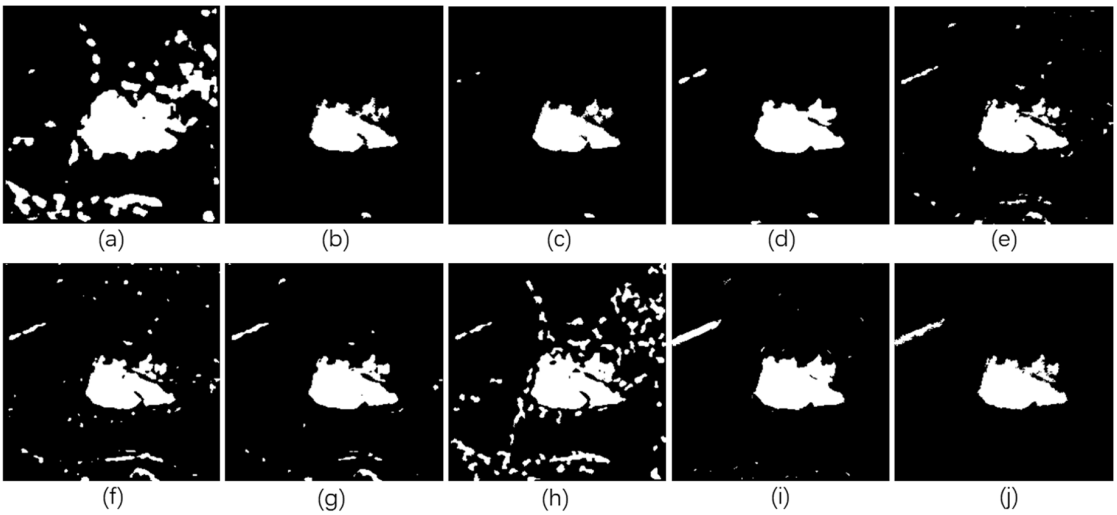


Figure 9. CD results of the San Francisco dataset. (**a**) PCAKM, (**b**) GarborPCA, (**c**) NBRELM, (**d**) CWNN, (**e**) DDNet, (**f**) LANTNet, (**g**) M2HG, (**h**) WBANet (**i**) PC-BiBL, and (**j**) ground truth.

To sum up, both qualitative and quantitative results demonstrate that the proposed PC-BiBL has superior performance in CD with SAR images. More specifically, the evaluation indexes OE, R, F1, OA, and KC of PC-BiBL are higher than these compared models in the five datasets. The value of R increases, but the value of P slightly decreases, which is a compromise in P and R. Furthermore, the change map of the proposed PC-BiBL has few isolated pixels to be mistakenly predicted as changed pixels. Moreover, PC-BiBL is skilled in detecting the changed areas and their edges.

4. Discussion

In the proposed PC-BiBL framework, the architectural design and parameter settings significantly influence the performance of CD with SAR images. To analyze the performance of CD, the Yellow River I dataset is adopted as an example for conducting experiments.

4.1. Analysis of PCConv

The PCConv is a critical component of PC-BiBL, responsible for extracting discriminative features. To investigate its contribution, the number of PCConv blocks is varied from 0 to 7, and the corresponding CD accuracies are summarized in Table 6. The results reveal that PC-BiBL without PCConv performs poorly, achieving the highest OE at 12,126, the lowest P at 0.5302, the lowest R at 0.8526, the lowest F1 at 0.6538, the lowest OA at 0.8367, and the lowest KC at 0.5545. In contrast, the inclusion of PCConv significantly improves performance, demonstrating its effectiveness in extracting deep and discriminative features for CD with SAR images. The optimal performance is achieved when the number of PCConv blocks is set to 2. This is attributed

to the ability of PCConv to extract hierarchical features containing both local and long-range information. While increasing the number of PCConv blocks enhances the extraction of deeper features, excessive use of long-range information can disrupt the CD task, which primarily relies on adjacent pixel relationships for accurate change prediction. By limiting the number of PCConv blocks to 2, PC-BiBL strikes a balance between capturing sufficient contextual information and preserving local details, making it highly effective for SAR images CD.

Table 6. CD results of analyzing the number of PCConv blocks (w/o denotes without PCConv).

Number of PCConv	OE	P	R	F1	OA	KC
w/o	12,126	0.5302	0.8526	0.6538	0.8367	0.5545
1	3070	0.8490	0.9383	0.8914	0.9587	0.8660
2	**2052**	**0.8904**	**0.9662**	**0.9267**	**0.9724**	**0.9097**
3	2336	0.8783	0.9589	0.9169	0.9685	0.8975
4	2499	0.8723	0.9536	0.9111	0.9664	0.8904
5	2535	0.8706	0.9529	0.9099	0.9659	0.8889
6	2593	0.8689	0.9503	0.9078	0.9651	0.8863
7	2698	0.8622	0.9512	0.9045	0.9637	0.8821

4.2. Analysis of Feature Channel in PCConv

In PCConv, the number of feature channels is directly related to the number of selected pseudo-random convolution kernels (k), which represents the quantity of deep features. Investigating the optimal number of feature channels is crucial for effectively leveraging the power of PCConv. Figure 10 presents the results of varying the number of feature channels from 10 to 130. It is notable that as the number of feature channels increases, the accuracies of CD first show an upward trend and then decline. This is because the model fails to fully utilize the available information, leading to sub-optimal performance. When the number of feature channels is set to 50, the CD results reach their peak. This indicates that the deep features obtained under this configuration are most suitable for the CD task, enabling the model to capture the necessary information effectively. However, when the number of feature channels exceeds 50, a decrease in accuracy is observed. This phenomenon suggests that an excessive number of feature channels may introduce redundant or overly complex information, which confounds the CD process rather than enhancing it. Based on the above-mentioned analysis, the number of feature channels in PCConv is set to 50. This value strikes the best balance between information utilization and model complexity, ensuring optimal performance in CD.

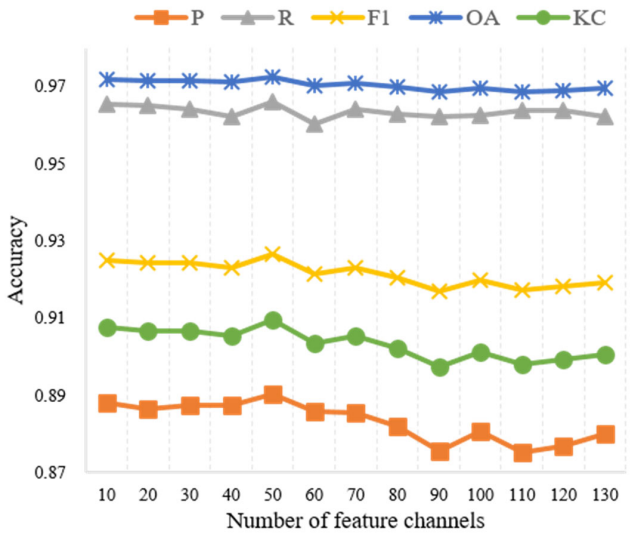


Figure 10. CD results of analyzing the number of feature channels in PCConv.

4.3. Analysis of Cross Convolution

The origin of convolution kernels can significantly impact the quality of the features extracted, thereby exerting a notable influence on the CD performance of the proposed PC-BiBL. To illustrate the effect of kernel source, the experiments of the source of convolution kernels are carried out for gaining useful deep features. The results of CD in Table 7 are acquired with different source cases of convolution kernel for convolution in PCConv as follows:

Case 1 Kernels of Conv1 and Conv2 both come from $\overline{P}^{t1}$, but kernels of Conv1 and Conv2 are different.

Case 2 Kernels of Conv1 and Conv2 both come from $\overline{P}^{t1}$, and kernels of Conv1 and Conv2 are the same.

Case 3 Kernels of Conv1 and Conv2 both come from $\overline{P}^{t2}$, but kernels of Conv1 and Conv2 are different.

Case 4 Kernels of Conv1 and Conv2 both come from $\overline{P}^{t2}$, and kernels of Conv1 and Conv2 are the same.

Case 5 Kernels of Conv1 come from $\overline{P}^{t1}$ and kernels of Conv2 come from $\overline{P}^{t2}$. The locations of kernels selected of Conv1 and Conv2 are different.

Case 6 Kernels of Conv1 come from $\overline{P}^{t1}$ and kernels of Conv2 come from $\overline{P}^{t2}$. The locations of kernels selected of Conv1 and Conv2 are the same.

Case 7 Kernels of Conv1 come from $\overline{P}^{t2}$ and kernels of Conv2 come from $\overline{P}^{t1}$. The locations of kernels selected of Conv1 and Conv2 are different.

Case 8 Kernels of Conv1 come from $\overline{P}^{t2}$ and kernels of Conv2 come from $\overline{P}^{t1}$. The locations of kernels selected of Conv1 and Conv2 are the same.

Case 9 Kernels of Conv1 and Conv2 both are randomly generated, but kernels of Conv1 and Conv2 are different.

Case 10 Kernels of Conv1 and Conv2 both are randomly generated, and kernels of Conv1 and Conv2 are the same.

Case 11 Kernels cross bi-temporal features. Half of kernels of Conv1 and Conv2 come from $\overline{P}^{t1}$, and the other half come from $\overline{P}^{t2}$. Kernels of Conv1 and Conv2 are different.

Case 12 PC-BiBL. Kernels cross bi-temporal features. Half of kernels of Conv1 and Conv2 come from $\overline{P}^{t1}$, and the other half come from $\overline{P}^{t2}$. Kernels of Conv1 and Conv2 are shared and the same.

Table 7. CD results of analyzing sources of kernels.

Sources	OE	P	R	F1	OA	KC
Case 1	2194	0.8839	0.9632	0.9218	0.9705	0.9038
Case 2	2322	0.8746	0.9655	0.9178	0.9687	0.8985
Case 3	2244	0.8786	0.9665	0.9204	0.9698	0.9019
Case 4	2203	0.8820	0.9652	0.9217	0.9703	0.9033
Case 5	2231	0.8782	**0.9682**	0.9210	0.9700	0.9026
Case 6	2373	0.8715	0.9657	0.9162	0.9681	0.8967
Case 7	2320	0.8779	0.9610	0.9175	0.9688	0.8984
Case 8	2178	0.8842	0.9641	0.9224	0.9707	0.9045
Case 9	9130	0.6125	0.8718	0.7195	0.8771	0.6439
Case 10	4650	0.7749	0.9215	0.8419	0.9374	0.8032
Case 11	2286	0.8768	0.9655	0.9190	0.9692	0.9000
Case 12	**2052**	**0.8904**	0.9662	**0.9267**	**0.9724**	**0.9097**

Conv1 denotes the convolution for feature $\overline{P}^{t1}$ and Conv2 denotes the convolution for feature $\overline{P}^{t2}$. Analyzing Case 9 and Case 10, it is evident that when the kernels are randomly

generated, the resulting CD performance is the least satisfactory. This finding strongly implies that kernels derived from the original features play a crucial role in effectively extracting deep features during the convolution process. Furthermore, when convolution kernels of Conv1 and Conv2 are the same and shared, crossing bi-temporal features which indicates taking half kernels from feature $\overline{P}^{t1}$, and the other half from feature $\overline{P}^{t2}$, the OE, P, F1, OA, and KC are superior compared to the kernels from other source cases. Thus, it indicates that the shared kernels of Conv1 and Conv2 crossing bi-temporal features are beneficial to obtain discriminative cross-features for subsequent CD.

4.4. Analysis of Pseudo-Random Kernel

Pseudo-random kernels are obtained by randomly selecting a pixel in each cluster after cluster all pixels, and then extracted with the same center locations of the selected pixels. To evaluate the performance of pseudo-random kernels for convolution, the results without a pseudo-random kernel where the center locations of extracted kernels are the same as of randomly selected pixels and with a pseudo-random kernel are displayed in Table 8. In the ablation study, w/o pseudo-random kernel refers to the PCConv configuration without pseudo-random kernel generation, whereas w/ pseudo-random kernel represents the variant that employs pseudo-random kernels. The experimental results clearly demonstrate that when pseudo-random kernels are employed in the PCConv convolution process, significant improvements are observed in several key performance metrics, including P, R, F1, OA, and KC. These findings demonstrate that pseudo-random kernels effectively increase kernel diversity and function similarly to learnable convolution kernels for feature extraction in PC-BiBL. Therefore, the proposed analysis provides quantitative evidence supporting both the rationale and stability of the pseudo-random kernel generation mechanism. Notably, the number of misclassified pixels in the model with pseudo-random kernels is 222 less than that in the model without pseudo-random kernels. This improvement can be attributed to the fact that the use of pseudo-random kernels effectively increases the diversity of the kernels. Therefore, pseudo-random kernels are as convolution kernels in PC-BiBL to extract features.

Table 8. CD results of analyzing the pseudo-random kernel.

Method	OE	P	R	F1	OA	KC
w/o pseudo-random kernel	2274	0.8791	0.9632	0.9192	0.9694	0.9004
with pseudo-random kernel	**2052**	**0.8904**	**0.9662**	**0.9267**	**0.9724**	**0.9097**

4.5. Analysis of Convolution Kernel Size in PCConv

Convolution kernel size as an important parameter in the proposed PC-BiBL is also analyzed. Table 9 shows the experimental results in different size of convolution kernel. We set the size as 3×3, 5×5, 7×7, 9×9, 11×11, 13×13, 15×15 and 17×17. The accuracy indexes P, F1, OA, and KC initially increase and then decrease as the kernel size grows, with the optimal performance achieved at a kernel size of 7×7. The R progressively increases as the kernel size increases. The visual experimental results of the proposed PC-BiBL with different kernel size are shown in Figure 11. As the kernel size increases, the number of isolated pixels falsely predicted as changes decreases and the edges of the change regions become more diffuse. This behavior can be attributed to the fact that larger kernels capture broader contextual information, which enhances the extraction of global features. However, this comes at the cost of overlooking local and subtle features, leading to a trade-off between global and local feature representation. Therefore, a kernel size of 7×7 strikes an optimal balance, enabling the proposed PC-BiBL to achieve superior performance for CD with SAR images.

Table 9. CD results of analyzing the convolution kernel size in PCConv.

Kernel Size	OE	P	R	F1	OA	KC
3 × 3	8905	0.6138	0.9089	0.7328	0.8801	0.6592
5 × 5	3730	0.8068	0.9497	0.8724	0.9498	0.8414
7 × 7	**2052**	**0.8904**	0.9662	**0.9267**	**0.9724**	**0.9097**
9 × 9	2296	0.8748	0.9675	0.9188	0.9691	0.8998
11 × 11	2324	0.8722	0.9690	0.9180	0.9687	0.8988
13 × 13	2483	0.8647	0.9663	0.9127	0.9666	0.8921
15 × 15	2688	0.8511	0.9695	0.9064	0.9638	0.8841
17 × 17	2917	0.8373	**0.9716**	0.8995	0.9607	0.8752

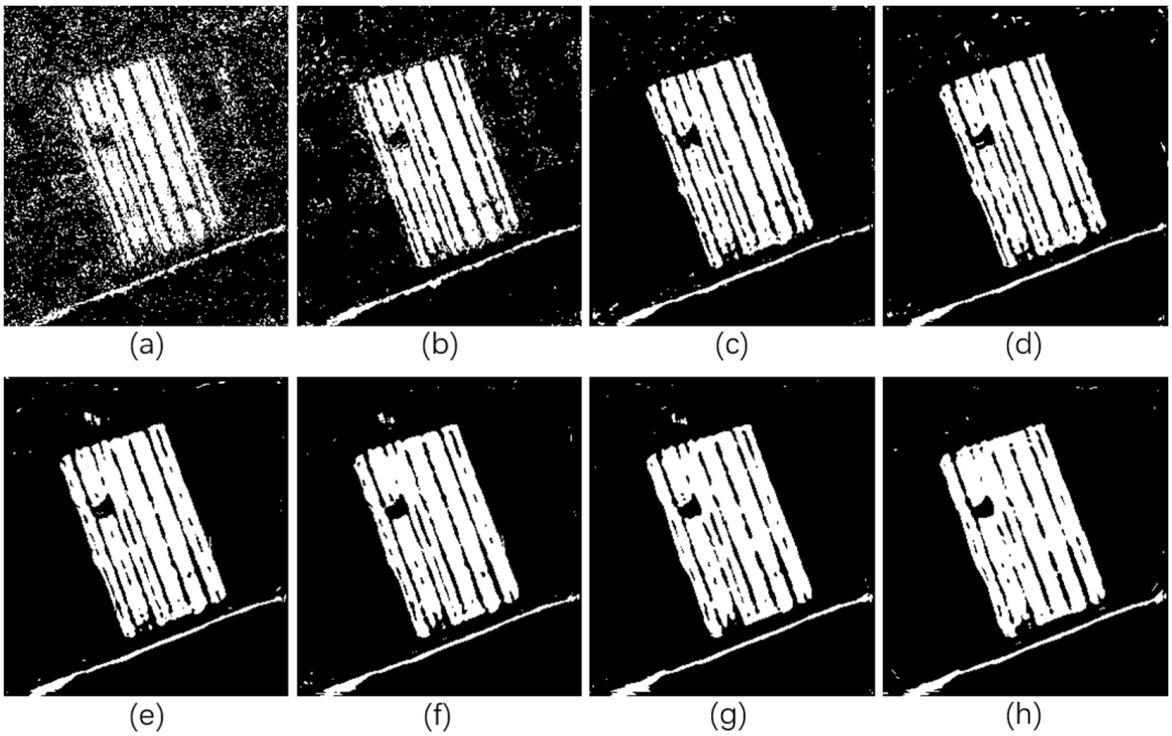


Figure 11. CD results of analyzing kernel size in PCConv. (**a**) 3 × 3, (**b**) 5 × 5, (**c**) 7 × 7, (**d**) 9 × 9, (**e**) 11 × 11, (**f**) 13 × 13, (**g**) 15 × 15, and (**h**) 17 × 17.

4.6. Analysis of Patch Size for BiBL Module

Patch size for the BiBL module is an important parameter that determines the amount of contained information. We set patch size as 3 × 3, 5 × 5, 7 × 7, 9 × 9, 11 × 11, 13 × 13, 15 × 15, and 17 × 17 for exploring the suitable patch size. The experimental results of the proposed PC-BiBL with different patch sizes are shown in Table 10 and in Figure 12. As the patch size gradually increases, a remarkable trend emerges: the number of misclassified isolated pixels in the CD results steadily decreases. This indicates that larger patches are more effective in capturing context-related information, thereby reducing the likelihood of misidentifying individual pixels. When delving into the accuracy metrics, a peak in performance is observed when the patch size is set to 11 × 11. At this configuration, the P reaches 0.8904, the R ascends to 0.9662, the F1 attains 0.9267, the OA climbs to 0.9724, and the KC reaches 0.9097. Therefore, for the proposed PC-BiBL, the amount of contained information in patch is suitable for CD with SAR images when patch size for the BiBL module is set as 11 × 11.

Table 10. CD results of analyzing the patch size for the BiBL module.

Patch	OE	P	R	F1	OA	KC
3 × 3	2467	0.8817	0.9429	0.9112	0.9668	0.8908
5 × 5	2539	0.8717	0.9509	0.9096	0.9658	0.8886
7 × 7	2485	0.8694	0.9591	0.9120	0.9665	0.8914
9 × 9	2248	0.8810	0.9626	0.9200	0.9697	0.9014
11 × 11	**2052**	**0.8904**	**0.9662**	**0.9267**	**0.9724**	**0.9097**
13 × 13	2185	0.8826	0.9658	0.9223	0.9706	0.9042
15 × 15	2348	0.8756	0.9618	0.9167	0.9684	0.8972
17 × 17	2279	0.8800	0.9614	0.9189	0.9693	0.9000

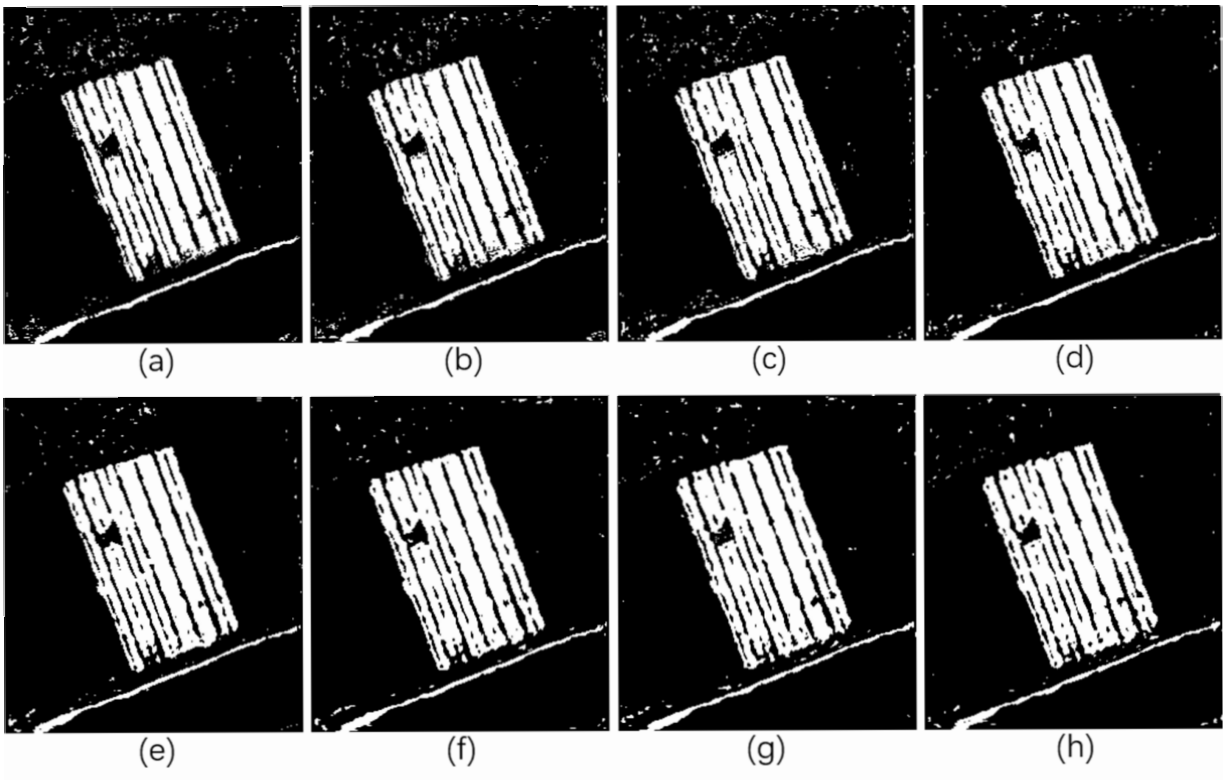


Figure 12. CD results of analyzing patch size. (**a**) 3 × 3, (**b**) 5 × 5, (**c**) 7 × 7, (**d**) 9 × 9, (**e**) 11 × 11, (**f**) 13 × 13, (**g**) 15 × 15, and (**h**) 17 × 17.

4.7. Analysis of the Number of Sparse Feature Nodes and Enhancement Nodes

The number of sparse feature nodes and enhancement nodes are two important parameters for improving the nonlinearity of features. Thus, the number of sparse feature nodes and enhancement nodes are also discussed in this paper, which are shown in Table 11. It is shown that the optimal number of sparse feature nodes and enhancement nodes is 4400 and 12,000, respectively. When the number of these nodes is relatively small, the model fails to effectively extract the latent information within the input data. This is because a limited number of nodes restricts the model's ability to capture diverse feature patterns, leading to sub-optimal performance. Conversely, an excessive number of nodes can also be detrimental. As the number of nodes increases beyond a certain threshold, the information density per node decreases. This results in a situation where the model struggles to generate substantial amounts of relevant information. Thus, setting the number of sparse feature nodes and enhancement nodes as 4400 and 12,000, respectively, the generated nodes are appropriate to feed to the output layer of the BiBL module.

Table 11. CD results of analyzing the number of sparse feature nodes and enhancement nodes.

Sparse Feature Nodes	Enhancement Nodes	OE	P	R	F1	OA	KC
400	6000	2802	0.8526	0.9567	0.9017	0.9623	0.8785
1200	6000	2340	0.8760	0.9620	0.9170	0.9685	0.8976
2000	6000	2344	0.8760	0.9616	0.9168	0.9684	0.8974
2800	6000	2283	0.8798	0.9614	0.9188	0.9693	0.8999
3600	6000	2323	0.8772	0.9617	0.9175	0.9687	0.8983
4400	6000	2383	0.8730	0.9626	0.9156	0.9679	0.8959
5200	6000	2273	0.8800	0.9619	0.9191	0.9694	0.9003
4400	8000	2320	0.8770	0.9623	0.9176	0.9688	0.8984
4400	10,000	2135	0.8865	0.9645	0.9239	0.9713	0.9062
4400	**12,000**	**2052**	**0.8904**	**0.9662**	**0.9267**	**0.9724**	**0.9097**
4400	14,000	2183	0.8836	0.9646	0.9223	0.9706	0.9042
5200	12,000	2280	0.8772	0.9655	0.9192	0.9693	0.9003
6000	12,000	2281	0.8794	0.9621	0.9189	0.9693	0.9000

4.8. Analysis of the Shared Weights for Dual Broad Nodes Generation

To validate the effectiveness of shared weights in the generation of dual broad nodes, we conducted experiments comparing two scenarios: (1) generating nodes in dual branches without shared weights and (2) generating nodes with shared weights. The CD results are displayed in Table 12. Notably, while PC-BiBL achieves a R of 0.8980 without shared weights, which is slightly higher than the R of 0.8904 with shared weights, the overall performance metrics, including OE, F1, OA, and KC, are significantly improved when shared weights are employed. This improvement can be attributed to the fact that shared weights ensure consistent processing of nodes in both branches, which facilitates the extraction of differential information from the dual nodes. Therefore, the use of shared weights in dual broad nodes generation enhances the model's ability to emphasize feature differences, thereby improving the accuracy of subsequent CD training and prediction.

Table 12. CD results of analyzing the shared weight.

Method	OE	P	R	F1	OA	KC
w/o shared weight	2189	**0.8980**	0.9443	0.9206	0.9705	0.9038
with shared weight	**2052**	0.8904	**0.9662**	**0.9267**	**0.9724**	**0.8985**

4.9. Analysis of the Influence of Speckle Noise in PC-BiBL

Speckle noise is a prevalent issue in SAR images, significantly affecting the accuracy of CD results. To evaluate the effectiveness of PC-BiBL in mitigating speckle noise interference, we compare its performance with variants of PC-BiBL that incorporate pre-processing denoising techniques, including median filtering (MF), lee filtering (LF), and non-local means denoising (NLMD). As illustrated in Figure 13, the change maps generated by PC-BiBL exhibit a comparable number of incorrectly predicted isolated pixels to those produced by PC-BiBL with MF, LF, and NLMD. This suggests that PC-BiBL inherently mitigates the influence of speckle noise without requiring additional denoising steps. Further insights into this phenomenon are provided in Figure 11, which demonstrates that increasing the convolution kernel size in PCConv reduces the number of erroneous isolated pixels. This reduction is attributed to the feature smoothing effect achieved by the PCConv operation, which functions similarly to a smoothing filter. As the kernel size increases, the smoothing effect becomes more pronounced, leading to enhanced noise suppression. In addition, the process of PCA, which reduces the dimensionality of cross-features, can also reduce speckle

noise. Consequently, PC-BiBL effectively addresses the challenge of speckle noise in SAR images, eliminating the need for explicit pre-processing denoising techniques.

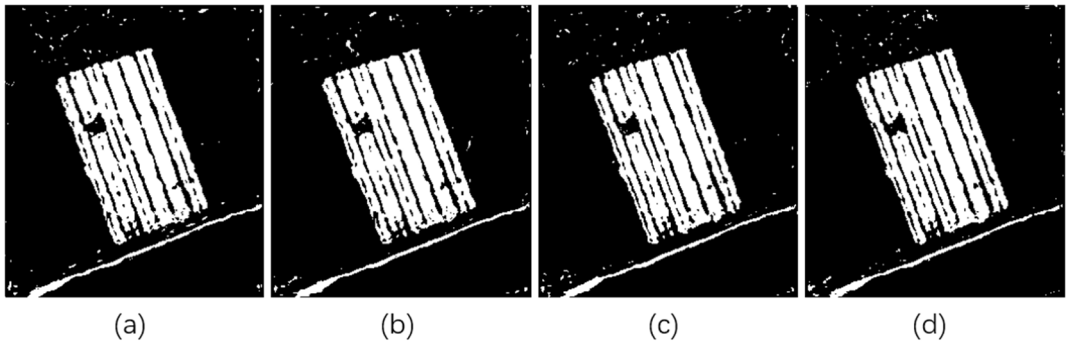


Figure 13. CD results of analyzing the influence of speckle noise. (**a**) MF, (**b**) LF, (**c**) NLMD, and (**d**) PC-BiBL.

4.10. Computational Efficiency and Interpretability Analysis

To provide a quantitative comparison of computational complexity, we measured the inference time and parameter count of the proposed PC-BiBL and compared methods Table 13. Methods with zero parameters are non-learnable and thus excluded from comparison.

Table 13. Computational complexity comparison.

Method	Inference Time(s)	Parameter Count
PCAKM	0.73	0
GarborPCA	612	0
NBRELM	**0.492**	6000
CWNN	36.4	**1230**
DDNet	3.42	10,312
LANTNet	0.55	27,836
M2HG	73.1	0
WBANet	13.5	7159
PC-BiBL	74.3	32,800

As shown in Table 13, although PC-BiBL exhibits a higher inference time and parameter scale than other methods, it has more stable and discriminative change detection performance. In particular, PC-BiBL consistently outperforms traditional training-free methods in terms of F1-score, overall accuracy (OA), and boundary integrity, especially in scenarios involving subtle changes, complex backgrounds, and speckle noise. Compared with deep learning-based methods, PC-BiBL achieves competitive detection performance without requiring any training process or labeled data. This indicates that its structural complexity is not a result of simple parameter stacking, but rather a necessary design choice tailored to the requirements of multi-scale change modeling and robust discriminative representation in remote sensing change detection tasks.

5. Conclusions

In this paper, we propose a novel framework, named PC-BiBL, to integrate the advantages of deep learning networks and BLSs for CD with SAR images. The framework consists of two key modules, i.e., a HCCE module and BiBL module. The HCCE module utilizes PCConv to extract discriminative features with spatial-temporal information. The designed PCConv is a unique convolution mechanism that operates without requiring

any training process. It adopts pseudo-random convolution kernels crossing bi-temporal features for convolution to explore correlations between bi-temporal images. This achieves feature smoothing and reducing noise. The BiBL module is designed to broaden hierarchical cross-features to improve the nonlinearity and robustness. Subsequently, this module analyzes the difference nodes derived from bi-temporal nodes, enabling better adaptation to CD with bi-temporal SAR images. Experimental results on five widely used datasets, i.e., Yellow River I, Yellow River II, Yellow River III, Sulzberger, and San Francisco, demonstrate great performance in CD compared to several state-of-the-art models.

The proposed framework demonstrates promising performance for bi-temporal SAR change detection. However, the current framework has limitations in capturing multi-source and multispectral information. First, the method assumes homogeneous input sources and is designed specifically for bi-temporal SAR imagery, which is not directly applicable to heterogeneous change detection scenarios, such as SAR–optical image pairs. Second, the proposed approach is tailored to bi-temporal, single-channel SAR images and is not appropriate to multispectral/hyperspectral data. In future work, we will extend the framework to address these challenges and enhance its applicability.

Author Contributions: Conceptualization, S.Y. and B.Y.; methodology, Z.W.; validation, S.Y., Z.W. and B.Y.; formal analysis, J.Q.; investigation, X.L.; writing—original draft preparation, S.Y. and L.L.; writing—review and editing, Z.W. and B.Y.; funding acquisition, Q.H. and B.Y. All authors have read and agreed to the published version of the manuscript.

Funding: This work was supported in part by the Young Outstanding Science and Technology Talents Cultivation Program (Science and Technology Talent Support Project) of Hunan Province, China under Grant 2023TJ-N16, in part by the Science and Technology Program of Hunan Province, China under Grant 2024RC3108, in part by the Natural Science Foundation of Hunan Province, China under Grant 2023JJ20018, 2024JJ8320, 2025JJ80020, and in part by the Key Research and Development Program of Hunan Province, China under Grant 2023SK2041.

Data Availability Statement: The datasets analyzed in this study are all publicly available. The original data is derived from existing remote sensing datasets, accessible via the following links: (1) Yellow River I, II, and III datasets at https://github.com/yulisun/INLPG/tree/master/datasets (accessed on 14 May 2025); (2) Sulzberger dataset at https://github.com/summitgao/SAR_Change_Detection_CWNN (accessed on 14 May 2025); (3) San Francisco dataset at https://github.com/DavidJimenezS/GBF-CD/tree/master/Data (accessed on 14 May 2025). All experimental results presented in the manuscript were obtained through standard preprocessing and analysis of these publicly available datasets. No new data was created in this work.

Conflicts of Interest: The authors declare that they have no known competing financial interests or personal relationships that could have appeared to influence the work reported in this paper.

References

1. Wang, X.; Du, P.; Liu, S.; Senyshen, M.; Zhang, W.; Fang, H.; Fan, X. A novel multiple change detection approach based on tri-temporal logic-verified change vector analysis in 696 posterior probability space. *Int. J. Appl. Earth Obs. Geoinf* **2022**, *111*, 102852. [CrossRef]
2. Tian, D.; Gong, M. A novel edge-weight based fuzzy clustering method for change detection in SAR images. *Inf. Sci.* **2018**, *467*, 415–430. [CrossRef]
3. Ghosh, A.; Mishra, N.S.; Ghosh, S. Fuzzy clustering algorithms for unsupervised change detection in remote sensing images. *Inf. Sci.* **2011**, *181*, 699–715. [CrossRef]
4. Jin, S.; Dewitz, J.; Li, C.; Sorenson, D.; Zhu, Z.; Shogib, M.R.I.; Danielson, P.; Granneman, B.; Costello, C.; Case, A. National Land Cover Database 2019: A Comprehensive Strategy for Creating the 1986–2019 Forest Disturbance Product. *J. Remote Sens.* **2023**, *3*, 0021. [CrossRef]
5. Jin, S.; Dewitz, J.; Danielson, P.; Granneman, B.; Costello, C.; Smith, K.; Zhu, Z. National Land Cover Database 2019: A new strategy for creating clean leaf-on and leaf-off Landsat composite images. *J. Remote Sens.* **2023**, *3*, 0022. [CrossRef]

6. Michel, U.; Mildes, W. Environmental monitoring in peat bog areas by change detection methods. *Earth Resour. Environ. Remote Sens. GIS Appl. VII SPIE* **2016**, *10005*, 448–454. [CrossRef]
7. Hame, T.; Heiler, I.; San Miguel-Ayanz, J. An unsupervised change detection and recognition system for forestry. *Int. J. Remote Sens.* **1998**, *19*, 1079–1099. [CrossRef]
8. Zheng, Z.; Zhong, Y.; Wang, J.; Ma, A.; Zhang, L. Building damage assessment for rapid disaster response with a deep object-based semantic change detection framework: From 46 natural disasters to man-made disasters. *Remote Sens. Environ.* **2021**, *265*, 112636. [CrossRef]
9. Shanthi, I.; Valarmathi, M. Speckle noise suppression of SAR image using hybrid order statistics filters. *Int. J. Adv. Eng. Sci. Technol.* **2011**, *5*, 229–235.
10. Ying, L.; Miao, D.; Zhang, Z. A robust one-stage detector for SAR ship detection with sequential three-way decisions and multi-granularity. *Inf. Sci.* **2024**, *667*, 120436. [CrossRef]
11. Yang, F.; Jiang, X.; Ziegler, A.D.; Estes, L.D.; Wu, J.; Chen, A.; Ciais, P.; Wu, J.; Zeng, Z. Improved fine-scale tropical forest cover mapping for Southeast Asia using Planet-NICFI and Sentinel-1 imagery. *J. Remote Sens.* **2023**, *3*, 0064. [CrossRef]
12. Su, H.; Zhang, X.; Luo, Y.; Zhang, C.; Zhou, X.; Atkinson, P.M. Nonlocal feature learning based on a variational graph auto-encoder network for small area change detection using SAR imagery. *ISPRS J. Photogramm. Remote Sens.* **2022**, *193*, 137–149. [CrossRef]
13. Xue, W.; Ai, J.; Zhu, Y.; Chen, J.; Zhuang, S. AIS-FCANet: Long-Term AIS Data Assisted Frequency-Spatial Contextual Awareness Network for Salient Ship Detection in SAR Imagery. *IEEE Trans. Aerosp. Electron. Syst.* **2025**, *61*, 15166–15171. [CrossRef]
14. Lu, Y. MSF-CNN: Multi-Scale Fusion Convolutional Neural Network for Tactile Acceleration Signal Classification. In Proceedings of the 2025 IEEE 5th International Conference on Computer Communication and Artificial Intelligence (CCAI), Haikou, China, 23–25 May 2025; pp. 218–223. [CrossRef]
15. Zhang, W.; Jiao, L.; Liu, F.; Yang, S.; Song, W.; Liu, J. Sparse feature clustering network for unsupervised SAR image change detection. *IEEE Trans. Geosci. Remote Sens.* **2022**, *60*, 5226713. [CrossRef]
16. Zhu, J.; Guo, Y.; Sun, G.; Yang, L.; Deng, M.; Chen, J. Unsupervised domain adaptation semantic segmentation of high-resolution remote sensing imagery with invariant domain-level prototype memory. *IEEE Trans. Geosci. Remote Sens.* **2023**, *61*, 5603518. [CrossRef]
17. Li, Y.; Zhang, Y.; Zhu, Z. Error-tolerant deep learning for remote sensing image scene classification. *IEEE Trans. Cybern.* **2020**, *51*, 1756–1768. [CrossRef]
18. Cai, X.; Li, B.; Wu, L.; Chang, T.; Zhang, W.; Chen, J. A dynamic interval multi-objective optimization algorithm based on environmental change detection. *Inf. Sci.* **2025**, *694*, 121690. [CrossRef]
19. Gao, H.; Yang, Y.; Li, C.; Gao, L.; Zhang, B. Multiscale residual network with mixed depthwise convolution for hyperspectral image classification. *IEEE Trans. Geosci. Remote Sens.* **2020**, *59*, 3396–3408. [CrossRef]
20. Liu, T.; Li, Y.; Cao, Y.; Shen, Q. Change detection in multitemporal synthetic aperture radar images using dual-channel convolutional neural network. *J. Appl. Remote Sens.* **2017**, *11*, 042615. [CrossRef]
21. Du, Y.; Zhong, R.; Li, Q.; Zhang, F. TransUNet++ SAR: Change detection with deep learning about architectural ensemble in SAR images. *Remote Sens.* **2022**, *15*, 6. [CrossRef]
22. Li, H.-C.; Yang, G.; Yang, W.; Du, Q.; Emery, W.J. Deep nonsmooth nonnegative matrix factorization network with semi-supervised learning for SAR image change detection. *ISPRS J. Photogramm. Remote Sens.* **2020**, *160*, 167–179. [CrossRef]
23. Luo, B.; Hu, C.; Su, X.; Wang, Y. Differentially deep subspace representation for unsupervised change detection of SAR images. *Remote Sensing* **2019**, *11*, 2740. [CrossRef]
24. Wang, R.; Wang, L.; Wei, X.; Chen, J.-W.; Jiao, L. Dynamic graph-level neural network for SAR image change detection. *IEEE Geosci. Remote Sens. Lett.* **2021**, *19*, 4501005. [CrossRef]
25. Chen, C.P.; Liu, Z. Broad learning system: An effective and efficient incremental learning system without the need for deep architecture. *IEEE Trans. Neural Netw. Learn. Syst.* **2017**, *29*, 10–24. [CrossRef]
26. Han, H.; Liu, Z.; Liu, H.; Qiao, J.; Chen, C.P. Type-2 fuzzy broad learning system. *IEEE Trans. Cybern.* **2021**, *52*, 10352–10363. [CrossRef] [PubMed]
27. Xu, L.; Chen, C.P.; Qing, F.; Meng, X.; Zhao, Y.; Qi, T.; Miao, T. Graph-represented broad learning system for landslide susceptibility mapping in Alpine-Canyon region. *Remote Sens.* **2022**, *14*, 2773. [CrossRef]
28. Tuerxun, W.; Xu, C.; Haderbieke, M.; Guo, L.; Cheng, Z. A wind turbine fault classification model using broad learning system optimized by improved pelican optimization algorithm. *Machines* **2022**, *10*, 407. [CrossRef]
29. Li, X.; Li, S.; Zhou, P.; Chen, G. Forecasting network interface flow using a broad learning system based on the sparrow search algorithm. *Entropy* **2022**, *24*, 478. [CrossRef]
30. Cao, X.-K.; Wang, C.-D.; Lai, J.-H.; Huang, Q.; Chen, C.P. Multiparty secure broad learning system for privacy preserving. *IEEE Trans. Cybern.* **2023**, *53*, 6636–6648. [CrossRef] [PubMed]
31. Feng, S.; Chen, C.P. Fuzzy broad learning system: A novel neuro-fuzzy model for regression and classification. *IEEE Trans. Cybern.* **2018**, *50*, 414–424. [CrossRef]

32. Chen, C.P.; Liu, Z.; Feng, S. Universal approximation capability of broad learning system and its structural variations. *IEEE Trans. Neural Netw. Learn. Syst.* **2018**, *30*, 1191–1204. [CrossRef] [PubMed]
33. Hu, X.; Wei, X.; Gao, Y.; Liu, H.; Zhu, L. Variational expectation maximization attention broad learning systems. *Inf. Sci.* **2022**, *608*, 597–612. [CrossRef]
34. Liu, L.; Cai, L.; Liu, T.; Philip Chen, C.L.; Tang, X. Cauchy regularized broad learning system for noisy data regression. *Inf. Sci.* **2022**, *603*, 210–221. [CrossRef]
35. Wang, D.; Chen, X.; Jiang, M.; Du, S.; Xu, B.; Wang, J. ADS-Net: An Attention-Based deeply supervised network for remote sensing image change detection. *Int. J. Appl. Earth Obs. Geoinf.* **2021**, *101*, 102348. [CrossRef]
36. Tuya. Graph convolutional enhanced discriminative broad learning system for hyperspectral image classification. *IEEE Access* **2022**, *10*, 90299–90311. [CrossRef]
37. Zhao, H.; Liu, S.; Du, Q.; Bruzzone, L.; Zheng, Y.; Du, K.; Tong, X.; Xie, H.; Ma, X. GCFnet: Global collaborative fusion network for multispectral and panchromatic image classification. *IEEE Trans. Geosci. Remote Sens.* **2022**, *60*, 5212614. [CrossRef]
38. Tu, B.; Wang, Z.; Ouyang, H.; Yang, X.; Li, J.; Plaza, A. Hyperspectral anomaly detection using the spectral–spatial graph. *IEEE Trans. Geosci. Remote Sens.* **2022**, *60*, 5542814. [CrossRef]
39. Li, X.; Zhang, L.; You, J. Domain transfer learning for hyperspectral image super-resolution. *Remote Sens.* **2019**, *11*, 694. [CrossRef]
40. Liu, L.; Cai, L.; Xie, T.; Wang, Y. Self-paced broad learning system. *IEEE Trans. Cybern.* **2022**, *53*, 4029–4042. [CrossRef]
41. Zhu, S.; Song, Y.; Zhang, Y.; Zhang, Y. ECFNet: A Siamese network with fewer FPs and fewer FNs for change detection of remote-sensing images. *IEEE Geosci. Remote Sens. Lett.* **2023**, *20*, 6001005. [CrossRef]
42. Gao, H.; Yang, Y.; Li, C.; Zhang, X.; Zhao, J.; Yao, D. Convolutional neural network for spectral–spatial classification of hyperspectral images. *Neural Comput. Appl.* **2019**, *31*, 8997–9012. [CrossRef]
43. Marukatat, S. Tutorial on PCA and approximate PCA and approximate kernel PCA. *Artif. Intell. Rev.* **2023**, *56*, 5445–5477. [CrossRef]
44. Wang, L.; Scott, K.A.; Xu, L.; Clausi, D.A. Sea ice concentration estimation during melt from dual-pol SAR scenes using deep convolutional neural networks: A case study. *IEEE Trans. Geosci. Remote Sens.* **2016**, *54*, 4524–4533. [CrossRef]
45. Yang, B.; Mao, Y.; Liu, L.; Liu, X.; Ma, Y.; Li, J. From trained to untrained: A novel change detection framework using randomly initialized models with spatial–channel augmentation for hyperspectral images. *IEEE Trans. Geosci. Remote Sens.* **2023**, *61*, 4402214. [CrossRef]
46. Xu, Y.; Du, B.; Zhang, F.; Zhang, L. Hyperspectral image classification via a random patches network. *ISPRS J. Photogramm. Remote Sens.* **2018**, *142*, 344–357. [CrossRef]
47. Ma, Y.; Liu, Z.; Chen, C.P. Multiscale random convolution broad learning system for hyperspectral image classification. *IEEE Geosci. Remote Sens. Lett.* **2021**, *19*, 5503605. [CrossRef]
48. Boemer, F.; Ratner, E.; Lendasse, A. Parameter-free image segmentation with SLIC. *Neurocomputing* **2018**, *277*, 228–236. [CrossRef]
49. Boyd, S.; Parikh, N.; Chu, E.; Peleato, B.; Eckstein, J. Distributed optimization and statistical learning via the alternating direction method of multipliers. *Found. Trends Mach. Learn.* **2011**, *3*, 1–122. [CrossRef]
50. Johnson, R.D.; Kasischke, E. Change vector analysis: A technique for the multispectral monitoring of land cover and condition. *Int. J. Remote Sens.* **1998**, *19*, 411–426. [CrossRef]
51. Celik, T. Unsupervised change detection in satellite images using principal component analysis and k-means clustering. *IEEE Geosci. Remote Sens. Lett.* **2009**, *6*, 772–776. [CrossRef]
52. Gao, F.; Dong, J.; Li, B.; Xu, Q. Automatic change detection in synthetic aperture radar images based on PCANet. *IEEE Geosci. Remote Sens. Lett.* **2016**, *13*, 1792–1796. [CrossRef]
53. Gao, F.; Dong, J.; Li, B.; Xu, Q.; Xie, C. Change detection from synthetic aperture radar images based on neighborhood-based ratio and extreme learning machine. *J. Appl. Remote Sens.* **2016**, *10*, 046019. [CrossRef]
54. Gao, F.; Wang, X.; Gao, Y.; Dong, J.; Wang, S. Sea ice change detection in SAR images based on convolutional-wavelet neural networks. *IEEE Geosci. Remote Sens. Lett.* **2019**, *16*, 1240–1244. [CrossRef]
55. Qu, X.; Gao, F.; Dong, J.; Du, Q.; Li, H.-C. Change Detection in Synthetic Aperture Radar Images Using a Dual-Domain Network. *IEEE Geosci. Remote Sens. Lett.* **2022**, *19*, 4013405. [CrossRef]
56. Meng, D.; Gao, F.; Dong, J.; Du, Q.; Li, H.-C. Synthetic aperture radar image change detection via layer attention-based noise-tolerant network. *IEEE Geosci. Remote Sens. Lett.* **2022**, *19*, 4026505. [CrossRef]
57. Wang, J.; Zeng, F.; Niu, S.; Zheng, J.; Jiang, X. SAR Image Change Detection via Heterogeneous Graph With Multiorder and Multilevel Connections. *IEEE J. Sel. Top. Appl. Earth Obs. Remote Sens.* **2024**, *17*, 11386–11401. [CrossRef]
58. Xie, J.; Gao, F.; Zhou, X.; Dong, J. Wavelet-Based Bi-Dimensional Aggregation Network for SAR Image Change Detection. *IEEE Geosci. Remote Sens. Lett.* **2024**, *21*, 4013705. [CrossRef]

Disclaimer/Publisher's Note: The statements, opinions and data contained in all publications are solely those of the individual author(s) and contributor(s) and not of MDPI and/or the editor(s). MDPI and/or the editor(s) disclaim responsibility for any injury to people or property resulting from any ideas, methods, instructions or products referred to in the content.